Center for the Advancement of Natural Discoveries using Light Emission

Vahan Petrosyan

The Study of the Collimation and Radiation Effects of the Electron Beam in Accelerators

Thesis

to take a candidate degree in physical and mathematical sciences A.04.20

“Charged Particle Beam Physics and Accelerator Technology”

Scientific supervisor:

Doctor of Physical and Mathematical Sciences

Vitali Khachatryan

Yerevan 2019

Introduction

Currently, both Free Electron Lasers [FEL] and electronic colliders operate with high-quality low emittance beams, and collimation systems are essential to get rid of beam halo[1-3]. A conventional collimator system proposed for linear colliders and FELs consists of a series of spoilers and absorbers that serve two different functions: they remove particles from the beam halo and protect downstream beam-line elements against miss-steered or off-energy beam pulses. Electron beam collimation is necessary in the FEL in order to remove halo and dark current particles in the linac, before they impact and eventually degrade precise fields of the undulator permanent magnets [4].

Collimators are used in FLASH and European XFEL to increase the electron beam quality by cutting off the beam halo [1-2]. Secondary radiation occurs when electron beam interacts with collimators, beam diagnostic devices, and residual gas. Analytical methods based on the empirical formulae [5] are suited for the calculation of the electron interaction with the vacuum chamber residual gas, fine wires or thin sheets. Particle-tracking codes can be used to simulate the passage of the particles through the matter when particle beam interacts with the collimator, beam chamber walls or large pieces of instrumentation [5].

In general, the beam leaving the linear accelerator can have a significant halo extending to large amplitudes, both transversely and longitudinally due to beam-gas Coulomb scattering, beam-gas bremsstrahlung, Compton scattering on thermal photons [6], linac wake fields. Halo can be produced by the beam source (electron gun). The halo generation, due to beam-gas Coulomb scattering, can be reduced by a higher accelerating gradient, since the process probability decreases rapidly with the rise of electron energy, while the halo formation occurs due to beam-gas bremsstrahlung and Compton scattering on thermal photons scales with the length of the accelerator [7].

The task of the beam collimation system of the electron linac-based FEL is to protect the undulator modules against the miss-steered beam and dark-current [8-9].Results obtained at FLASH FEL facility have demonstrated that without collimation

halo particle causes demagnetization of the undulator permanent magnets very quickly for kW beam powers.

The study sets the objective to investigate the produced secondary radiation properties through numerical simulation when the electron beam particles hit collimator walls [10]. Using particle tracking simulation code FLUKA, the European XFEL electron beam, as well as beam halo interaction with the collimator, were simulated [11,1]. The complex geometrical shape and the material composition of the collimator have been taken into account. Absorbed dose spatial distribution in the material of the collimators and particle fluencies from the downstream surface of the collimator was simulated for the total secondary radiation and its main components.

The objective of the given study is the simulation of the produced secondary radiation properties when the electron beam halo particles hit collimator walls [12]. Using particle tracking simulation code, FLUKA the European XFEL electron beam interaction with the titanium collimator and copper absorber of the undulator intersections as well as FLASH beam interaction with the tapered collimator have been simulated. Absorbed dose spatial distribution in the material of the collimators was simulated for the total secondary radiation and its important photon and neutron components. After irritation of the collimator material by the electron beam and residual dose rate was calculated.

Advanced Research Electron Accelerator Laboratory (AREAL) is a 50 MeV electron linear accelerator project with a laser-driven RF gun, being constructed at the CANDLE Synchrotron Research Institute [13]. In addition to applications in life and materials sciences, the project aims at serving as a test facility for advanced accelerator and radiation source concepts. This work presents the AREAL RF photo-injector performance, the facility design considerations and its highlights in the fields of free electron laser, the study of new high frequency accelerating structures, the beam micro-bunching, and wake-field acceleration concepts.

The AREAL linear accelerator will produce an electron beam with 5 MeV energy and further upgrade up to $50\ MeV$ [14]. The construction of the beam diagnostic section

of complex shape and layout is planned at the first stage of the operation, thus making the radiation source definition difficult. FLUKA particle tracking simulation code was used to calculate produced radiation dose rates and define an appropriate radiation shielding.

The interaction of the AREAL photoelectron gun beam with the matter was simulated applying Particle tracking software [15]. The produced secondary particle fluxes produced at the certain places of interest within the AREAL facility experimental hall were calculated utilizing the data obtained by the electron beam diagnostic system; particularly, Faraday Cups (FC) and YAG screen stations. Absorbed dose rate has been measured by high precision ion chamber dosimeter, capable to measure radiation produced by the high-frequency pulsed source. The comparison of the simulation and dose measurement results allows validation of the calculation methods and beam diagnostic data. Particularly, ion chamber measurement of the dose creates an opportunity to estimate the beam energy spread more accurately.

The AREA Laser-driven RF gun provides 2–5 MeV energy ultra-short electron pulses for experimental study in life and materials sciences [16]. Ports were the first experimental results of the AREAL beam application in the study of molecular-genetic effects, silicon-dielectric structures, ferroelectric nano-films, and single crystals for scintillators.

An important part of the work concerns the study of the ~5 MeV electron beam interaction with the thin layer experimental sample at the AREAL electron linear accelerator [17]. The necessary exposure time and the irradiation effect parameters calculations have been performed using measured parameters of the beam and numerical simulations applying particle transport code FLUKA [11]. Numerical simulations with FLUKA provide the estimation of the absorbed dose - the main parameter that defines the amount of the radiation-induced crystalline structure defects. Calculations have been conducted for the experimental study of the irradiation effects on the parameters of the ferromagnetic composition $Ba_{75}Sr_{25}TiO_3$ - Barium-Strontium-Titanate (BST) thin film. The main goal reached is the calculation of the required

exposure time taking into account beam intensity, energy, spatial and angular distributions, and experimental sample geometrical shape, size, composition, and disposition for obtaining the intended value of the absorbed dose. Beam parameters used for numerical simulations have been obtained from beam diagnostic measurements.

The thesis consists of an introduction, four chapters, a summary, and a bibliography. The introduction presents a short review of the actuality of problems and the main outcomes of the thesis.

The **first** chapter of study is devoted to the beam halo research, using computer simulation of the high energy electron beam interaction with collimators at FLASH and European XFEL. The beam collimation systems are applied to get rid of beam halo. The XFEL main collimator CL.COLM(4 collimators) is a system consisting of 4 Titanium alloy tubes (diameters are 4, 6, 8 and 20 mm) distributed vertically, internal pure Al block and outer Copper block(length=50cm) with brazed cooling tubes[18]. The collimator with its movers will be located inside the steel housing (length=1m), in a vacuum. In numerical calculations with FLUKA, only the main characteristics of geometry have been taken into account. Therefore, somewhat simplified geometry was used in calculations, which includes only the main collimator block, steel housing and beam pipe (with 40.5mm diameters). The thickness of the titanium tubes and beam pipe wall is 2 mm. All tubes (0.5m long) are not tapered. Vertical direction movers enable the usage of any of four aperture of the collimator. The general view does not correspond to the exact final design.

Collimators are used in FLASH and European XFEL to cut off electron beam halo [1,2]. Secondary radiation is emitted when electron beam interacts with collimators, beam diagnostic devices, and residual gas. Analytical methods based on the empirical formulae [5] are suited for the calculation of the electron interaction with the vacuum chamber residual gas, fine wires or thin sheets. Particle-tracking codes can be used to simulate the passage of the particles through the matter, when particle beam interacts with the collimator, beam chamber walls or large pieces of instrumentation. We will use

FLUKA to simulate the interaction of the electron beam with the FLASH and European XFEL collimators made of Titanium and Copper [11].

Radiation study applying particle simulation code is instrumental for validation of the collimators material and geometry choices. It also gives an opportunity to design an appropriate shielding to protect personnel and prevent the radiation damage of the sensitive equipment and electronics.

The results of the simulations of the beam impact on the collimator wall show that downstream to collimator outside beam pipe dose rate (Dose-Equivalent) reaches to a few Pico Sieverts ($\leq 10\ pSv$) per primary electron.

In order to find the effectiveness of the collimator in reducing a beam halo were stimulated the interaction of the two different types of halo with the collimator. The parameters of the electrons coming out from the downstream surface of the collimator were transferred to the entrance of the next collimator at the EXFEL collimator section using linear transfer matrices.

The **second** chapter of the thesis is devoted to AREAL linear accelerator 5 MeV electron beam interaction with the matter. AREAL uses laser-driven RF gun based on electron linear accelerator project aiming to produce small emittance ultra-short electron beam pulses for advanced experiments. It is capable of producing 5 MeV beam with beam current equal to 200 pC [19]. Along with laser-driven RF gun two acceleration structures will permit electron beam energy to reach the energy of 20 MeV and further up to 50 MeV.

The second chapter of the study concerns to the radiation safety calculations at AREAL facility and near premises, since secondary radiation sources rose due to the interaction of the beam electrons with the matter of beam dump target, vacuum chamber walls, beam detectors, and diagnostic equipment. Radiation doses are calculated applying FLUKA particle tracking code [11]. Concrete walls of the machine tunnel as well as movable shielding walls constructed of Led and concrete bricks contribution to radiation level outside of tunnel well below the natural background.

The secondary radiation has been generated when the electron beam interacts with the material on the beam trajectory (beam dump target, beam pipe walls, detectors and beam diagnostic equipment). In the current study low energy electron beam interaction with matter has been investigated by means of applying both numerical simulation and experimental measurement methods. For the determination of radiation field (radiation dose and its spatial and angular distribution in the AREAL machine hall and neigh boring rooms) by computer simulation of the beam interaction with matter has been performed along with the direct measurement of the radiation dose rates. FLUKA Monte Carlo particle transport code has been used [20,21]. The radiation dose simulations using digital simulation computer codes are necessary for the design and development of the adequate radiation shielding and for the planning of the radiation protection measures in the stages of the particle accelerator construction, operation and update. The choice of the FLUKA code is based on the consideration that an operational up to date version of the code is available and FLUKA gives an opportunity to track the particles to the low energies consuming reasonably affordable computational resources and time.

Both calculation data based on numerical simulation and dose measurements proved that radiation dose levels in the AREAL machine hall and experimental rooms were under the control and completely conform to the radiation safety requirements for equipment and personnel.

It is shown that the insertion of 10 cm Led shielding around dump reduces the concrete thickness to 50 cm. It also includes the contingency that takes into account possible deviations of the concrete parameters from the design values, e.g. density, homogeneity, isotropy, and chemical composition. Dose measurements by high precision ion chamber dose meter have been carried out and satisfactory agreement between measurement results and the numerical simulation results has been found. Safety requirements in the AREAL machine hall and experimental rooms for equipment and personnel in AREAL up to 5MeV energies are confirmed.

The **third** chapter of the given dissertation is devoted to the material irradiation related scientific research experiments at the AREAL linear accelerator applying low energy electron beam. Due to small emittance ultra-short electron beam pulses, AREAL is attractive for a wide range of advanced experimental studies such as radiobiology, molecular physics, solid-state physics, and microelectronics. The usage of the AREAL electron beams in the fields of life and materials sciences is an important issue for exploiting the facility's full potential and its development.

An experimental study has been carried out at the AREAL linear accelerator aiming at the investigation of the effect of the irradiation by the 4.2 MeV electron beam on the electrical properties of the ferroelectric composition $Ba_{75}Sr_{25}TiO_3$ (BST). Ferroelectric thin films, particularly BS-based ones, have wide applications in multifunctional microelectronic devices [22-23]. The electric, dielectric, and Ferro-electric characteristics of these thin films can be modified via electron irradiation leading to microelectronic devices new performance [24–28]. The BST thin films have a low-frequency dependence of the relative permittivity and dielectric losses. Those dependencies can be substantially changed by the samples electron irradiation producing thin films with the properties adapted to the requirements of the application. The 4 MeV electron beam irradiation effects on the electric, dielectric, and ferroelectric properties of the BST film-based sensor have been studied in the frequency range from 100 Hz to 1 MHz's.

The paper is focused on the methods of the calculation of experimental sample irradiation parameters based on beam parameters measurement and numerical simulation study of the electron beam interaction with the BST material thin layer.

FLUKA simulations have been conducted aimed at the calculation of the required exposure time to provide necessary irradiation dose for the given beam parameters (energy, current, spatial sizes and divergence). Input parameters for FLUKA simulations of the electron beam interaction with experimental sample have been defined relying on two sets of the data. Beam diagnostic measurements results have been combined with

the sample geometrical and composition parameters. Calculated absorbed dose spatial distribution within the volume of the BST thin film has turned to be essentially uniform

The main outcomes of the dissertation are the following:

- The European XFEL electron beam interaction with the complex shape collimators and copper absorbers in the undulator intersections as well as FLASH FEL beam interaction with the tapered collimator were simulated applying particle tracking simulation code FLUKA.
- The simulations results indicate that two collimators (out of 4 installed) are enough to get rid of the halo entering the collimator section effectively.
- The results of the simulations of the beam impact on the collimator wall show that downstream to single collimator outside beam pipe dose rate (Dose-Equivalent) reaches to a few Pico Sieverts (≤10 pSv) per primary electron.
- The results of digital simulations of the FLASH FEL beam interaction with the tapered collimator yield data that have been useful for efforts toward the minimization of the degradation effect of radiation on the undulator permanent magnet blocks.
- FLUKA simulations of the secondary radiation field at AREAL machine hall and experimental rooms have been performed. Input parameters for the simulated beam have been derived from the beam diagnostic measurements.
- Dose rate measurement results have been compared with the values of numerical simulations and satisfactory agreement has been found thus validating the choice of simulation method.
- Dose measurement data were used to improve the accuracy of the beam diagnostic data. It was found particularly that the beam initial energy spread was about 1.5%.
- Numerical simulation and dose measurement gave data allowing development of the necessary radiation shielding and protection walls to ensure that radiation dose levels in the AREAL machine hall and experimental rooms conform to the radiation safety requirements for equipment and personnel.

- FLUKA simulations has been conducted aimed at calculation of the required exposure time to provide necessary irradiation dose for the given beam parameters (energy, current, spatial sizes and divergence).
- Beam diagnostic measurements results have been combined with the experimental sample geometrical and composition parameters and digital simulations of the electronic beam interaction with the experimental equipment have been performed.
- Absorbed dose spatial distributions within the volume of the experimental samples have been found via digital simulations. Calculated absorbed dose spatial distribution within the volume of the BST thin film has turned to be essentially uniform.

The study outcomes have been reported at international conferences, during the seminars at CANDLE Synchrotron Research Institute, Yerevan State University, DESY and are published in various scientific journals.

Chapter 1: Particle Tracking Simulation Study of the Electron Beam Interaction with the DESY FLASH and EXFEL Collimators Systems

1.1 Introduction

The objective of the study presented is the investigation of the produced secondary radiation properties when the electron beam particles hit collimator walls.

Using particle tracking simulation code, FLUKA the European XFEL electron beam interaction with the titanium collimator and copper absorber in the undulator intersections as well as FLASH beam interaction with the tapered collimator was simulated.

Absorbed dose spatial distribution in the material of the collimators was simulated for the total secondary radiation and its important components gamma and neutron components. The energy spectrum of the produced total radiation and its photon, neutron components were calculated. Angular and spectral double differential distributions of the radiation energy emitted by collimator surfaces were obtained.

Residual dose rate after irritation of the collimator material by the electron beam was found.

Analytical methods based on the empirical formulae [5] are suited for the calculation of the electron interaction with the vacuum chamber residual gas, tin wires or thin sheets. Particle-tracking codes can be used to simulate the passage of the particles through the matter when particle beam interacts with the collimator, beam chamber walls or large pieces of instrumentation. FLUKA software package have been applied to simulate the interaction of the electron beam with the FLASH and European XFEL collimators [11].

Bremsstrahlung radiation occurs when an electron beam interacts with collimators, beam diagnostic devices, and residual gas. Although electrons interact with

matter through various mechanisms (ionization, Moller scattering, bremsstrahlung, electron-positron pair production, etc.) in a few GeV energy region bremsstrahlung is the leading process. An important of objective the current study is the calculation of the effects of the electron beam interaction with the medium since bremsstrahlung radiation overlaps with the FEL radiation and it is necessary to evaluate bremsstrahlung contribution to the total radiation at the undulator exit. Since there is a rather long strait part of the beam vacuum chamber next to the undulator section, bremsstrahlung photons produced at any point may reach beam line end. Produced bremsstrahlung radiation can cause unwanted heat loads when incident on the instrumentation pieces downstream.

Bremsstrahlung causes beam energy losses and widens beam energy spread, thus degrading FEL performance. Actually, an electron can lose its entire energy in the single bremsstrahlung event.

In some cases, electron beam encounters with enough amount of the material allowing several interaction events to occur. That process takes place when beam interacts with the collimators, screens with slits, windows frames, etc. In the case of the beam incident on the collimator or beam pipe wall an electromagnetic shower can be developed. In those cases, interaction process should be studied applying full-featured particle tracking simulation codes. In the case of the beam impact on the beam scanner thin wire or vacuum chamber residual gas molecules, only one interaction act takes place and analytical approach suffices.

1.2 Energy Loss by Electrons

Electrons interact with material through several mechanisms:

Ionization $\mathrm{e}^- + \mathrm{A} \rightarrow \mathrm{e}^- + \mathrm{A}^+ + \mathrm{e}^-;$

Moller scattering $\mathrm{e}^- + \mathrm{e}^- \rightarrow \mathrm{e}^- + \mathrm{e}^-$;

Bremsstrahlung $\mathrm{e}^- + \mathrm{e}^-(\mathrm{A}) \rightarrow \mathrm{e}^-(\mathrm{A}') + \gamma;$

Pair production $\mathrm{e}^- + \mathrm{e}^-(\mathrm{A}) \rightarrow \mathrm{e}^-(\mathrm{A}') + (\mathrm{e}^+ + \mathrm{e}^-);$

etc.

Electron (positron) scattering is considered as ionization when the energy loss per collision is below $0.255\ MeV$, and as Möller's (Bhabha) scattering when it is above.

At high energies (starting from a few tens of MeVs) bremsstrahlung mechanism prevails.

1.3 Energy loss by ionisation (electron and positron)

In collisions of charged particles with a matter occurring excitation and ionization. Energy loss during bremsstrahlung must also be considered for relativistic particles. Interacting neutral particles must produce charged particles, which are then detected during their specific interaction processes. For photons these processes are known as Compton scattering, photoelectric effect and pair production of electrons. The electron can be observed through a sensitive ionization detector, which is generated during photon interactions.

Exact calculation taking into account the specific differences between the incident heavy particles and electrons gives a more accurate formula for the loss of electron energy as a result of ionization and excitation [29].

$$-\frac{dE}{dx} = 4\,\pi\,N_A r_e^2 m_e c^2 \frac{Z}{A}\cdot\frac{1}{\beta^2}\left(\ln\frac{\gamma m_e c^2 \beta\sqrt{\gamma-1}}{\sqrt{2}I} + \frac{1}{2}(1-\beta^2) - \frac{2\gamma-1}{2\gamma^2}\ln 2 + \frac{1}{16}\left(\frac{\gamma-1}{\gamma}\right)^2\right) \tag{1.1}$$

This expression agrees with the general Bethe–Bloch relation within $10\%-20\%$. The kinematics of electron-electron collisions and screening effects also it takes into account.

The treatment of the ionisation loss of positrons is similar to that of electrons if one considers that these particles are of equal mass, but not identical charge.

For completeness, we also give the ionisation loss of positrons [30]:

$$-\frac{dE}{dx} = 4\,\pi\,N_A r_e^2 m_e c^2 \frac{Z}{A}\cdot\frac{1}{\beta^2}\left(\ln\frac{\gamma m_e c^2 \beta\sqrt{\gamma-1}}{\sqrt{2}I} - \frac{\beta^2}{24}\left[23 + \frac{14}{\gamma+1} + \frac{10}{(\gamma+1)^2} + \frac{4}{(\gamma+1)^3}\right]\right) \tag{1.2}$$

Since positrons are antiparticles of electrons, there is, however, an additional consideration: if positrons come to rest, they will annihilate with an electron normally into two photons which are emitted anticollinearly. Both photons have energies of $511\ keV$ in the centre-of-mass system, corresponding to the rest mass of the electrons. The cross section for annihilation in flight is given by [30]

$$\sigma(Z,E) = \frac{Z\pi r_e^2}{\gamma+1}\left[\frac{\gamma^2+4\gamma+1}{\gamma^2-1}\ln\left(\gamma+\sqrt{\gamma^2-1}\right) - \frac{\gamma+3}{\sqrt{\gamma^2-1}}\right] \quad (1.3)$$

More details about the ionisation process of elementary particles, in particular, its spin dependence, can be taken from the books of Rossi and Sitar et al. [31-33].

1.4 Energy loses by $e^{\pm}$ via collision

For electrons and positrons, stopping power is different from stopping the power of heavy particles. The difference is kinematics, charge, spin and the characteristics of the electron that causing ionization. A large part of electron's energy transfers to atomic electrons (taken as free), which is described by the Møller cross section. In a single collision the maximum energy transition equals to total kinetic energy $W_{max} = m_e\, c^2\, (\gamma\ -\ 1)$, but in case of identical particles, the maximum is half of this at $W_{max}/2$. (The results will be the same if transferred energy equals ϵ or $W_{max} - \epsilon$. The stopping power calculation is done for the faster of the two emerging electrons by convention). In the formula provided below stopping power is the first moment of the Møller cross section [34] (divided by dx)

$$\left\langle -\frac{\mathrm{dE}}{\mathrm{dx}}\right\rangle = \frac{1}{2}\mathrm{K}\frac{\mathrm{Z}}{\mathrm{A}}\frac{1}{\beta^2}\left[\ln\frac{\mathrm{m_e c^2}\beta^2\gamma^2\{\mathrm{m_e c^2}(\gamma-1)/2\}}{\mathrm{I^2}} + (1-\beta^2) - \frac{2\gamma-1}{\gamma^2}\ln 2 + \frac{1}{8}\left(\frac{\gamma-1}{\gamma}\right)^2 - \delta\right] \quad (1.4)$$

By substituting a logarithmic term in the Bethe equation by $W_{max} = m_e\, c^2(\gamma - 1)/2$ it can be compared with the logarithmic part in the formula shown above. The two forms differ by $\ln 2$. For describing electron-positron scattering a more complicated cross sectional formula called Bhabha cross section is used [34]. The identical particle problem doesn't exist in this case so we can consider that $W_{max} = m_e\, c^2\, (\gamma\ -\ 1)$. The first moment of the Bhabha equation results to the following.

$$\langle -\frac{dE}{dx} \rangle = \frac{1}{2} K \frac{Z}{A} \frac{1}{\beta^2} \left[\ln \frac{m_e c^2 \beta^2 \gamma^2 \{m_e c^2 (\gamma - 1)\}}{2I^2} + 2 \ln 2 - \frac{\beta^2}{12} \left(23 + \frac{14}{\gamma+1} + \frac{10}{(\gamma+1)^2} + \frac{4}{(\gamma+1)^3} \right) - \delta \right] \quad (1.5)$$

Density effect correction δ was added to Uehling's equations [34] by following ICRU 37 [35] in both cases.

According to **Figure 1.1** stopping powers for e^-, e^+ and heavy particles do not differ dramatically. In silicon material, the minimum value for e^- is $1.50 MeV\ cm^2/g$ (at $\gamma = 3.3$); for positrons, $1.46 MeV\ cm^2/g$ (at $\gamma = 3.7$), and for μ^- $1.66 MeV\ cm^2/g$ (at $\gamma = 3.58$).

1.5 Radiation Length

High-energy electrons interact with matter, mainly by bremsstrahlung while high-energy photons interact by electron-positron pair production. The characteristic amount of matter, traversed by those particles is called the radiation length X_0 (measured in gram cm^{-2}). The radiation length is the mean distance over which a high-energy electron loses all but $1/e$ of its energy by bremsstrahlung. Equivalently, it is the 7/9 part of the mean free path for pair production by a high-energy photon [36]. For high-energy electromagnetic cascades, the radiation length is also suitable. In **Eq. (1.6)** it is shown X_0 calculation which is tabulated by Y.S. Tsai [37]:

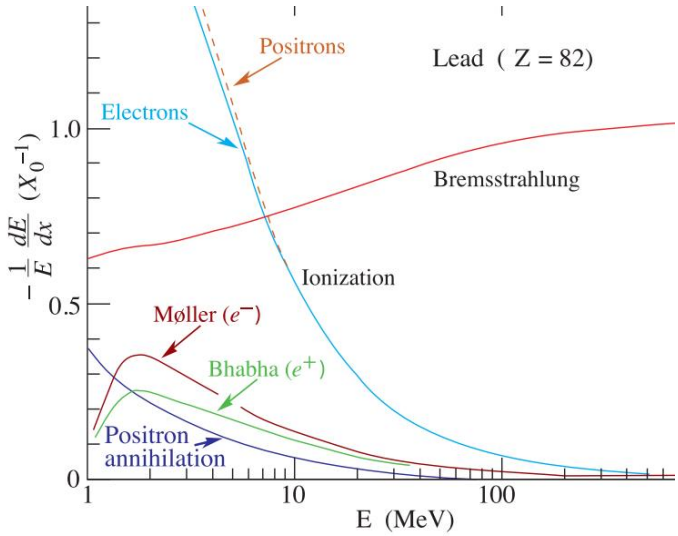

Figure 1.1: Fractional energy loss per radiation length in lead as a function of electron or position energy.

$$\frac{1}{X_0} = 4\alpha r_e^2 \frac{N_A}{N}\{Z^2[L_{rad} - f(Z)] + ZL'_{rad}\} \tag{1.6}$$

For $A = 1\ g\ mol^{-1}$, $4\alpha r_e^2\ N_A/A = (716.408\ g\ cm^{-2})^{-1}$. L_{rad} and L'_{rad} are given in **Table 1.1**. The function $f(Z)$ is an infinite sum. All elements up to uranium can be represented to 4-place accuracy by the following formula

$$f(Z) = a^2[(1 + a^2)^{-1} + 0.20206 - 0.0369a^2 + 0.0083a^4 - 0.002a^6]$$

where $a = \alpha Z$ [38].

For the mixed compound radiation, the length can be approximated by the following formula $1/X_0 = \sum w_j/X_j$ where w_j and X_j are the fractions by weight and the radiation length for the j-th element.

Although there are accurate formulae to calculate, O. I. Dahl provides a compact fit to the data [5]:

$$X_0 = \frac{716[g{-}cm^{-2}]A}{Z(Z+1)\ln(287/\sqrt{Z})} \tag{1.7}$$

where A is the atomic mass and Z is the atomic number of the absorber.

Table 1.1. Tsai's L_{rad} and L'_{rad} for use in calculating the radiation length Eq.(1.6)

Element	Z	L_{rad}	L'_{rad}
H	1	5.31	6.144
He	2	4.79	5.621
Li	3	4.74	5.805
Bi	4	4.71	5.924
Others	> 4	$\ln(184.5\, Z^{-1/3})$	$\ln(1194\, Z^{-2/3})$

Results obtained using this formula agree with Tsai's accurate formulae to better than 2.5% for all elements. The radiation associated with the mixture or compound may be approximated by the formula $1/X_0 = \sum w_i/X_{oi}$, where w_i and $X_{oi}$are the fractions by weight and the radiation length for the $i-th$ element.

1.6 Bremsstrahlung

A bremsstrahlung loses rate of electron energy is nearly proportional to its energy, while the ionization loss rate varies only logarithmically depending on electron energy. The critical energy E_c is sometimes defined as the energy at which the two loss rates are equal. The value of the critical energy when bremsstrahlung starts to prevail over ionization mechanism can be obtained by the expressions: $E_c = \frac{610MeV}{Z+1.24}$ for solids and liquids and $E_c = \frac{710MeV}{Z+0.92}$ for the gases. Alternatively, Rossi [39] defines the critical energy as the energy at which the ionization loss per radiation length is equal to the energy of electron. Experimental results prove that Rossi's form of the critical energy definition describes transverse electromagnetic shower development more accurately [5].

Bremsstrahlung radiation is emitted when the fast-moving charged particle is decelerated in the Coulomb field of the atoms. Though radiation takes place mainly due to the field of the nuclei, atomic electrons also contribute to the process. Since the probability of the bremsstrahlung process is proportional to the $1/M^2$ (M is the mass of the particle), starting from a few tens MeV, bremsstrahlung becomes the dominant process in the interaction of lightest charged particles electrons and positrons with the

most materials. Bremsstrahlung process probability increases with the Z^2 (Z is the atomic number).

Bethe-Heitler formula gives the energy loss rate

$$-\frac{dT_e}{dx} = n\,T_e\,\alpha\,Z^2 r_e^2\left(4\ln\frac{183}{Z^{1/3}}+\frac{2}{9}\right) \tag{1.8}$$

where n is the concentration of the atoms, α is the fine structure constant, $r_e = e^2/(m_e c^2)$ and it is assumed, that the electrons' kinetic energy $T_e \gg m_e c^2/\left(\alpha\,Z^{1/3}\right)$. This condition ensures consideration of the full screening effect. The electron cloud of the atoms contributes to the bremsstrahlung proportional to Z. Radiation spectrum calculation cannot be accurate without taking into account the co-called LPM effect [5].

The bremsstrahlung spectrum cross section approximation in the “complete screening case” at high energies can be done by the formula [37]

$$d\sigma/dk = (1/k)4\alpha\,r_e^2\left\{\left(\frac{4}{3}-\frac{4}{3}y+y^2\right)\left[Z^2(L_{rad}-f(Z)+ZL'_{rad}\right]+\frac{1}{9}(1-y)(Z^2+Z)\right\} \tag{1.9}$$

where $y = k/E$ is the part of the electron’s energy transferred to the radiated photon. At small y which is the case of “infrared limit” the term on the second line varies from 1.7% (low Z) to 2.5% (high Z) of the total/ If it is neglected and the first line shortened with the definition of X_0 given in **Eq. (1.6)**, we have

$$\frac{d\sigma}{dk} = \frac{A}{R\,N_A\,k}\left(\frac{4}{3}-\frac{4}{3}y+y^2\right) \tag{1.10}$$

Top curve in **Figure 1.2** shows cross this section (times k). This formula takes place except for the point $y = 1$ and $y = 0$. In $y = 1$ case, screening may become incomplete, and $y = 0$ case, infrared divergence is removed by the interference of bremsstrahlung amplitudes from nearby scattering canters (the LPM effect) [40,41] and dielectric suppression [42,43].

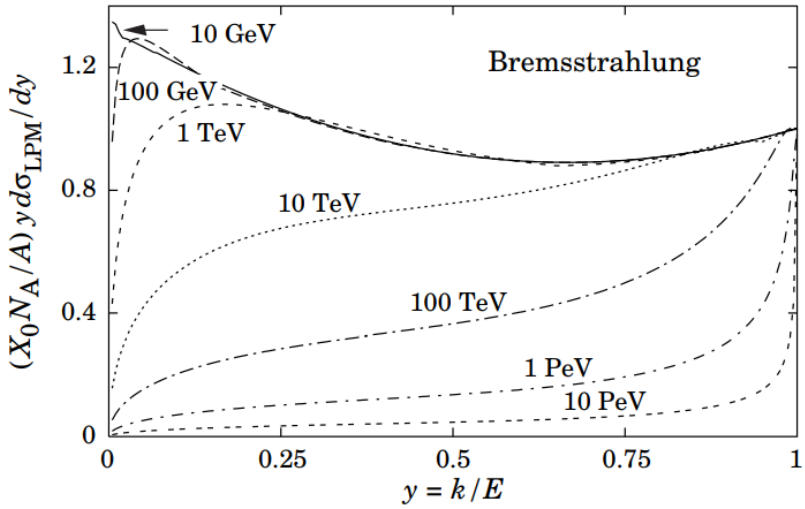

Figure 1.2: Dependence of the normalized bremsstrahlung cross section k $d\sigma_{LPM}/dk$ versus the fractional photon energy $y = k/E$ in lead. The vertical axis's unit containsis photons per radiation length.

One can obtain the expression for the energy loss rate $-\mathrm{dE/dx} = \mathrm{E/X_o}$. Thus, energy loss per unit path length is proportional to the energy of the charged particle and charged particle energy attenuation takes place exponentially:

$$\mathrm{E(x)} = \mathrm{E(0)}\exp(-\mathrm{x/X_0}) \tag{1.11}$$

The number of photons with energies between $\mathrm{k_1}$and $\mathrm{k_2}$radiated by an electron traveling a distance $\mathrm{d} \ll \mathrm{X_0}$ is

$$\mathrm{N_\gamma} = \frac{\mathrm{d}}{\mathrm{X_0}}\left[\frac{4}{3}\ln\left(\frac{\mathrm{k_2}}{\mathrm{k_1}}\right) - \frac{4\,(\mathrm{k_2}-\mathrm{k_1})}{3\,\mathrm{E_e}} + \frac{\mathrm{k_2^2}-\mathrm{k_1^2}}{2\mathrm{E_e^2}}\right] \tag{1.12}$$

The mean value of the photon emission in the bremsstrahlung process does not depend on the photon energy. It can be found from the formula

$$\bar{\vartheta} = \frac{\mathrm{m_e c^2}}{\mathrm{E_e}} \tag{1.13}$$

1.7 Electromagnetic Cascade

When thick absorber is hit by high-energy electron or photon it initiates an electromagnetic cascade as pair production and more electrons and photons with lower energy are generated by bremsstrahlung. The cascade evolution in the longitudinal direction is governed by the high-energy particles and therefore scales as the radiation

length in the material. Electrons' energy decreases and falls below the critical energy, and later dissipates it by ionization and excitation rather than by the creation of more shower particles. It is convenient in describing electromagnetic showers behavior to bring up the scale variables $t = x \,/\, X_0$; $y = E \,/\, E_c$. With this convention, distance is measured in units of radiation length and energy in units of critical energy.

In **Figure 1.3**, longitudinal profiles are shown from the simulation of a 30 GeV electron-induced cascade in iron by EGS4 [44]. The number of secondary particles which are crossing a plane (very close to Rossi's Π function [45]) is depends very sensitively on the cutoff energy, here chosen as the a total energy of $1.5\ MeV$ for both e^- and e^+. The number of electrons decreases more drastically than energy deposition. This happens because when increasing the depth at a larger portion of the cascade the energy is carried by photons. Calorimeter measurement depends on the device characteristics, but however, it is not likely to be exactly any of the profiles shown in **Figure 1.1**. In case of gas- based counters, it may be very close to the electron number, but in case of glass- based "Cherenkov" detectors, which have "thick" sensitive regions, it is closer to the energy deposition (total track length). In "Cherenkov" detectors, the detectors the signal is proportional to the "detectable" track length T_d which is in usually less than the total track length T. Real devices are sensitive to particles with energy higher than some threshold E_d, and $T_d = T\,F(E_d/E_c)$. An analytic formula for $F(E_d/E_c)$ is obtained by Rossi [45] is given by Fabjan in [46]; see also Amaldi [47].

The energy deposition mean longitudinal profile in an electromagnetic cascade is described in details by a gamma distribution [48]:

$$\frac{dE}{dt} = E_0 b \frac{(bt)^{a-1} e^{-bt}}{\Gamma(a)} \tag{1.14}$$

The maximum t_{max} occurs at $(a-1)/b$. Fits to shower profiles in elements from carbon to uranium, at energies from $1\ GeV$ to $100\ GeV$. The energy deposition profiles are well described by **Eq. (1.14)** with

$$t_{max} = (a-1)/b = 1.0 \times (\ln y + C_j)\,, \quad j = e, \gamma \tag{1.15}$$

where $C_e = -0.5$ for electron-induced cascades and $C_\gamma = +0.5$ for photon-induced cascades. To use **Eq. (1.14)**, one finds $(a - 1)/b$ from **Eq. (1.15)**, then finds a either by considering $b \approx 0.5$ or by finding a more accurate value **Figure 1.4**.

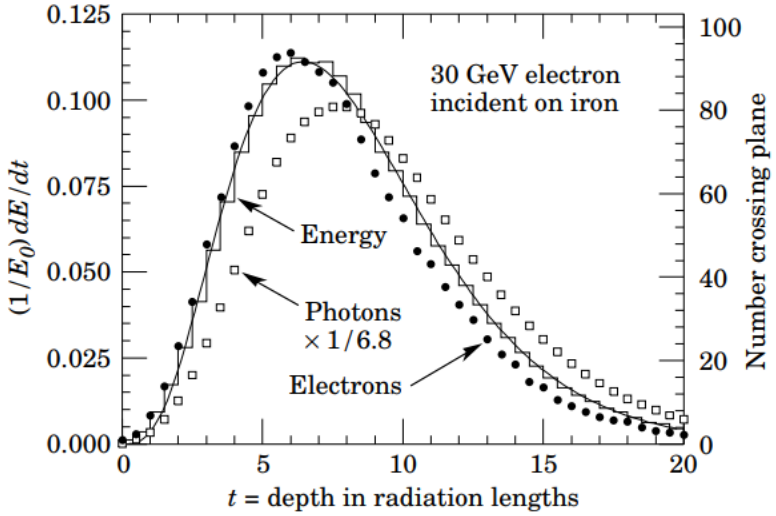

Figure 1.3: 30 GeV electron-induced cascade simulation in iron. Fractional energy deposition per radiation length is shown by the histogram, and the curve is a gamma-function fit to the distribution.

The results are identical for the electron number profiles, but it depends on the atomic number of the medium. The same form for the electron number maximum was obtained by Rossi in the assumption, but with $C_e = -1.0$ and $C_\gamma = -0.5$; we regard this as superseded by the EGS4 result.

Parameterization of "shower length" $X_s = X_0/b$ is done less conveniently, since b depends upon both Z and incident energy, as shown in **Figure 1.4**. As a consequence of this Z dependence, the number of electrons that are crossing a plane near shower maximum is underestimated using the approximation of Rossi for carbon and significantly overestimated for uranium. Necessarily the same b values are obtained for incident e^- and e^+. For most cases, it is sufficient to take $b \approx 0.5$.

Ultra-high energy photons and electrons have a greater length of showers than at lower energies since the first or first few lengths of interaction are increased by the mechanisms described above.

Near the origin, the EGS4 cascade (or a real cascade) increases more sharply, whereas the gamma function distribution is very flat. As a result (**Eq. 1.14**) fails abominably. For the first two radiation lengths cases; it was necessary to remove this region in making fits.

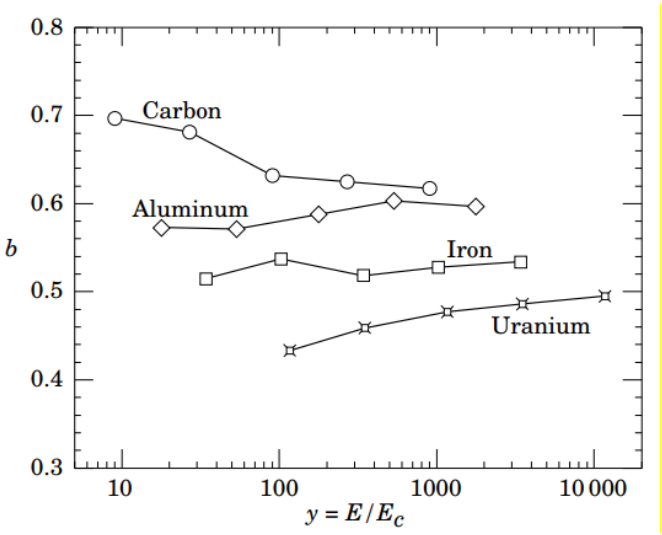

Figure 1.4: Scale factor b fit values for energy deposition profiles for a variety of elements for incident electrons with $1 \leq E_0 \leq 100\, GeV$.

Since fluctuations play an important role, (**Eq.1.14**) should be used only in applications where mean behavior is adequate. Fast simulation algorithms were developed by Grindhammer et al. in which the fluctuation and correlation of a and b are obtained by mapping (**Eq. 1.14**) to individually simulated cascades. Then from the correlated distributions [49] generated profiles for cascades using a and b were chosen.

The development of electromagnetic showers in the transverse direction in different materials scales quite accurately with the Moliere radius R_M, given by [50,51] $R_M = X_0\ E_s\ /\ E_c$, where $E_s \approx 21\, MeV$, and the Rossi definition of E_c is used.

In a material with weight fraction w_j of the element, with radiation length X_j and critical energy E_{cj}, the Moliere radius is expressed by

$$\frac{1}{R_M} = \frac{1}{E_s}\sum \frac{w_j E_{cj}}{X_j} \tag{1.16}$$

Lateral distribution measurements in electromagnetic cascades are depicted in [50,51]. On the average, only 10% of the electrons' energy lies outside the cylinder with

radius R_M. About 99% falls inside of $3.5R_M$, but at this radius and beyond composition effects play an important role and the scaling with R_M fails. The distributions are represented by a narrow core, and broaden as the shower develops. They are often represented as the sum of two Gaussians, and Grindhammer [49] definses them with the function

$$f(r) = \frac{2rR^2}{(r^2+R^2)^2} \tag{1.17}$$

where R is a phenomenological function of x/X_0 and $\ln E$. The LPM effect reduces the cross sections for bremsstrahlung and pair production at high energies and hence can cause significant elongation of electromagnetic cascades [41].

1.8 Simulation Methods

In modern particle physics, Monte Carlo simulations and the corresponding software packages are of essential importance, as they can help to understand the underlying physical processes of measured data or estimate physical quantities without measuring. As far as computer power increased, simulation time decreased and allowed to perform particle shower calculations for radiation safety studies also in complex geometries within the reasonable time. Within the scopes of the given thesis paper, the FLUKA Monte Carlo code [11,45] was used for radiological estimations and is, therefore, discussed more in detail in the following paragraphs.

1.9 FLUKA

In the given thesis, the FLUKA code [11, 52] was used to perform all the simulations. FLUKA is a Monte Carlo based simulation program specialized for particle physics related problems. FLUKA is a particle transport calculation tool and it has a wide range of applications where particles interact with matter, for example, electron accelerator shielding, dosimetry related problems, detector design, radiotherapy, cosmic rays, activation, neutrino physics, Accelerator Systems, radiobiology.

It was developed and is maintained under an INFN-CERN agreement. The highest priority of the FLUKA support team is improving and keeping it up to date with the current development of physics models. Modern physical models are continuously considered in the design and development of FLUKA.

Microscopic models are considered whenever possible.

Conservation laws are taken into account and consistency among all the reaction types and steps is ensured at each step of the calculation. FLUKA verifies all results against experimental data after each interaction of particles.

Finally, all predictions are obtained using a minimal set of parameters fixed for all energy/projectile/target combinations. As a result, in complex cases, scaling laws and properties originate from the underlying models of physics. When no experimental data are available, FULKA predicts the outcome of interaction event by taking into account correlations within interactions.

The FLUKA physical models are explained in a number of journals and conference publications [53-56]; on the technical side, the focus has been put on four obviously conflicting requirements, such as efficiency, accuracy, flexibility, and consistency. FLUKA can simulate with high precision the interaction and transportation in a matter of about 60 different particles such as electrons and photons from 1 keV to thousands of TeV, muons of all energies, hadrons of any energy up to 20 TeV, neutrinos and all the antiparticles, heavy ions and neutrons with the thermal energies. FLUKA package can also transport optical photons and polarized photons of synchrotron radiation. Tracking of emitted radiation and time evolution from unstable residual nuclei is calculated online.

FLUKA can handle from simple up to very complex geometrical setups. It uses an improved version of popular Combinatorial Geometry (CG) package. The CG of FLUKA has been programmed to track precisely also charged particles in the presence of electric and magnetic fields. Various visualization and debugging tools are also available. For most cases, no programming skills are required from the user. However,

a number of so-called user interface routines (using Fortran 77) are available for use with special requirements (FLUKA, 2010).

For many years, FLUKA has been known as one of the main tools for designing shielding of proton accelerators in the multi-GeV energy range (its hadron event generator has been adopted by the majority of the existing high-energy transport codes, including those used for particle physics simulations). In the recent years, however, FLUKA has gone through an important process of transformation, which has converted it from a specialized to a multi-purpose program, not restricted to a limited family of particles or to a particular energy domain. If in its original high energy field FLUKA has few competitors, this is not the case in the intermediate and low energy range, where several well-established transport codes exist. However, FLUKA can compare favourably with most of them, thanks to some important assets. One of them is the adoption of modern physical models, especially in the description of nuclear interactions. Some of these models have even been updated and extended with original contributions. Other advantages are the special care devoted to low-energy electromagnetic effects and the accurate combined treatment of multiple scattering and magnetic fields near material boundaries, essential for a correct simulation of many synchrotron radiation problems[56]. In the recent years, FLUKA has been widely used in the medical field to study different kinds of applications [57-61]: even if FLUKA has been validated in the high energy range [62,63], no specific validations in the energy range of medical application have been published. As the following chapters of the given work show, a careful validation of FLUKA, in terms of physical and transport parameters, was conducted in the energy range of interest in the medical field.

FLUKA reads user input from an ASCII text file. The input consists of a number of “commands” (which are called “options”), each consisting of one to multiple “lines” (which are called “cards” for historical reasons). Each card contains one keyword (the name of the command), six floating-point values called WHATs and one character string called SDUM. The specific structure of a FLUKA input file requires using the following [11]:

- Titles (labels) and comments used for documenting input file (which is optional, but recommended)
- Description of the setup geometry (bodies and surfaces), (required)
- Detailed specification of the materials (required, if pre-defined materials are used it can be omitted)
- Material correspondence (assigning materials to a region, required)
- Defining particle source (required)
- Defining of the requested “detectors”. Each detector is a phase space domain (particle energy and direction, the region of space) where one wants to simulate the probable value of a physical quantity, for example, dose, energy deposition, fluence, etc.
- Defining biasing schemes (optional)
- Defining problem settings (energy cut-offs, step size), physical effects not required for calculation by default, particles to be omitted during transportation, etc. (optional)
- Setup of the random number sequence (required if a statistical error estimation is requested)
- Starting condition and number of requested runs (required)

Additionally, special commands are available for more complex problems involving magnetic and electric fields time-dependent calculations, logging of history files (which are called “collision tapes”), optical photons transport, event-by-event scoring, calling custom-written routines, etc.

FLUKA offers several different built-in estimators, which are available directly from the input file. FLUKA users can request scoring the built-in available quantities they are interested in.

In the presented work DEFAULT card with NEW-DEFA option was used in all calculations and photonuclear interactions were activated via PHOTONUC card. Filters are defined (with AUXSCORE cards) in order to filter calculated quantities by particles, in this case, by neutrons and photons.

- USRBIN scoring card with generalized particle type DOSE used in order to calculate dose distribution in space.
- Average differential fluence as a function of energy in a given region was calculated using USRTACK card with the generalized particle type ENERGY.
- Double differential distributions of particles' energy and angle across a boundary surface of the target were calculated using USRBDX card with the generalized particle type ENERGY.

The residual dose rate was calculated by the one-step method using RADDECAY, IRRPROFI, DCYSCORE, DCYTIMES cards.

1.10 Flair

Flair [64] is an advanced graphical (user interface) UI for FLUKA, to enable the user to control FLUKA tasks completely using GUI environment with no need for command-line use. Flair is an integrated development environment (called shortly IDE) for FLUKA. It gives functionality for the post-processing of the output file. A big focus has been set on the creation and debugging of error-free input files. It includes a fully featured UI for modifying the input files in a human-friendly way with syntax checking, without hiding the native functions of FLUKA from the users. FLAIR also provides tools for building the executable, geometry debugging, code running, monitoring the status of many runs, output files inspection, binary files post-processing (e.g. data merging) and UI to plotting results like Gnuplot and PovRay in **Figure 1.5**.

It also includes a built-in database of selected properties of all so far known nuclides and their known isotopic structure as well as a database of ~250 predefined

materials with their physical parameters [64]. The program is also provided with a built-in Geometry Editor that allows for working on 2D cross-sections of the geometry, the visual editing of the 2D geometry interactively, debugging of bodies/regions in a graphical way and a fast 3D rendering of the geometry.

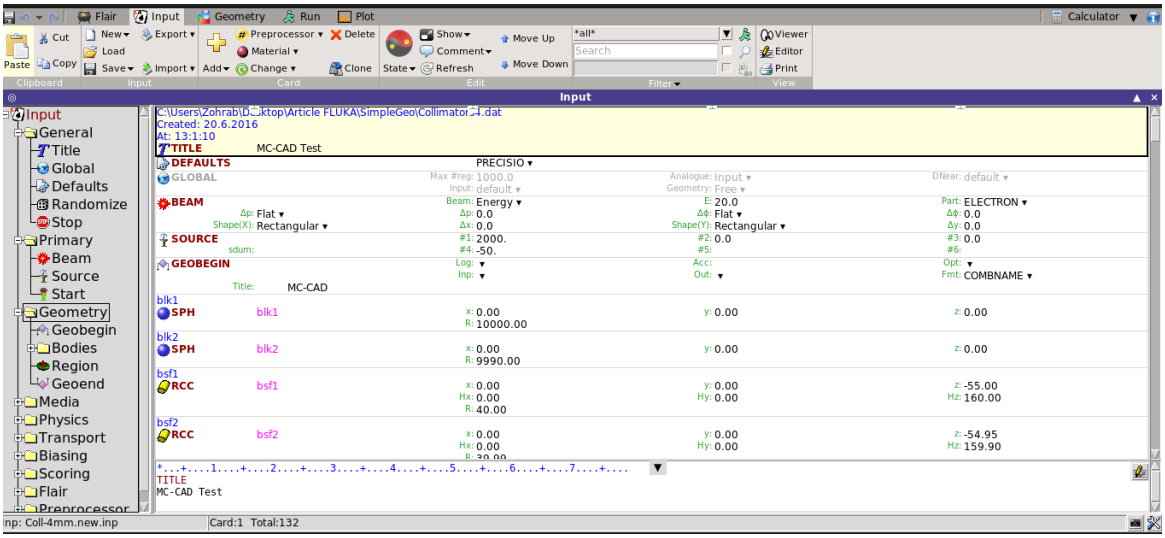

Figure 1.5: The FLUKA graphical interface Flair (v 2.0-8).

1.11 SimpleGeo

SimpleGeo [64] is an interactive 3D solid modelling program, which enables the flexible and easy creation of the geometric models via drag & drop UI, as well as on-the-fly debugging. The program includes new debugging means, based on stochastic and deterministic methods, in order to verify the created geometry with instant visual feedback of problematic regions. While the developing and the maintenance of Flair are strictly connected to the development of FLUKA, SimpleGeo is an independent project developed at CERN and specifically created to unify the various geometry modelling processes and syntaxes of radiation transport codes. Furthermore, even if with the last releases of Flair the potential of the geometry editor was continuously increased, SimpleGeo still remains very helpful in the developing of complex geometries.

Building geometries for particle tracking problems is one of the large time-consuming tasks. The main approach of radiation tracking codes is based on Constructive Solid Geometry (CSG), and textual input is required. This makes the

building of models a boring and error-prone task, which is particularly hard to master for beginner users. The program allows the user to build geometries in interactive mode using several basic objects, which are connected by Boolean operations. SimpleGeo has a native scripting language, which enables and facilitates parametric modelling. This scripting language has access to all parts of the modelling kernel and lets the user implement custom specific functionality himself. The program currently allows for importing as well as viewing of FLUKA. In addition to that, the user can build geometries from scratch and export to FLUKA. A number of plugins are under development to extend the functionality of SimpleGeo beyond solid modelling. The plugins (e.g. 3rd party extensions for SimpleGeo) used in the given dissertation paper are the DaVis3D, which enable for displaying data of physical quantities obtained from FLUKA simulation on top of the geometry **Figure 1.6**.

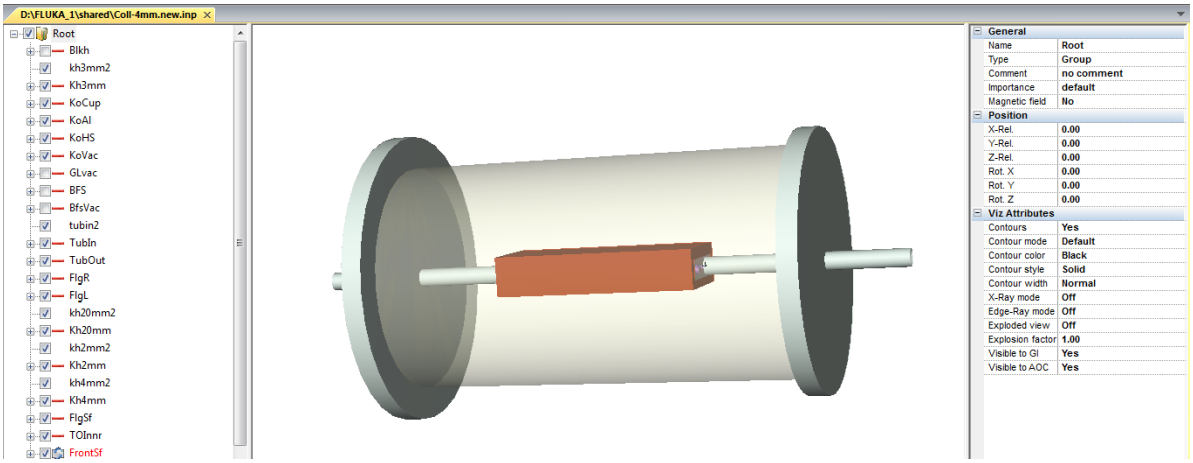

Figure 1.6: Interface of the 3D digital modeller SimpleGeo (v 4.3.3).

1.12 Beam Halo

After originating in the injector the electron beam has to be manipulated continually. It is required in order to ensure that it follows the desired trajectory. The components used to manipulate the electron beam in the beam pipe are the bending, corrector and focusing magnets. For circulation of electron beam bending magnets are

used while focusing magnets are used to direct the electron beam envelope towards the propagation axis.

Some portion of created electrons will not be contained within the core electron beam. Some of them will exist between the beam pipe inner surface and the core beam outside surface volume as shown in **Figure 1.7**. These electrons are called as halo electrons. The interaction of these electrons with the beam line equipment will create an intense radiation field. Because these particles' interaction is taking place at high energies (>7 MeV), more significant photon and neutron radiation will be created.

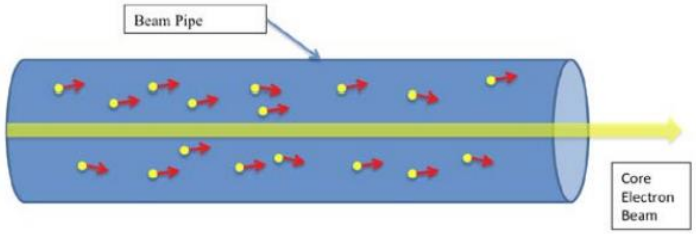

Figure 1.7: Halo Electrons outside core beam

The halo particles can travel along the pipe to the beam dump located at the end of the electron beam pipe. But some halo particles do not reach the beam dump. They interact with accelerator components and can produce a significant amount of radiation that is harmful to both the equipment and personnel.

All of the physical mechanisms that generate halo electrons are not fully understood. The distance between halo electrons and core electron beam can vary from a few rms beam radii to $10\ rms$ beam radii [65].

One of the potential sources for halo electrons is the scattering of drive laser light at the injector cathode. The surface quality of the cathode can also contribute to the amount of scattering, especially in the area near the edge of the emitter, and can be a significant contributor to the generation of halo electrons.

The transport of the halo electrons depends on the position and angle of the electrons within the beam line. Together these parameters define the phase space of the electrons during the transport through the FEL components. The radius, r_b, in phase

space is the distance of one electron from the center of the beam line. Each electron also has an angle, θ_b, with respect to the beamline axis. **Figure 1.8** shows how the halo electrons can exist outside of the core electron beam in the phase space.

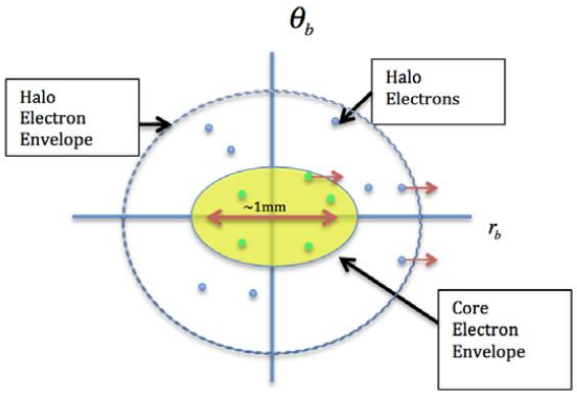

Figure 1.8: Core and halo electron beam phase space

The envelope of electron positions and angle can be related to the normalized transverse emittance parameter, given by [66]

$$\varepsilon_n = \gamma\, r_b \theta_b \tag{1.18}$$

where γ is the Lorentz factor, r_b is the core rms electron beam radius, and θ_b is the rms electron beam angle.

1.13 Beam Halo Particles Hit Collimator

The European XFEL, currently under construction at DESY (Germany), is a free-electron laser (FEL) based on self-amplified spontaneous emission (SASE) in the X-ray regime. The FEL consists of a 17.5 GeV superconducting electron linear accelerator and a set of undulators (**Figure 1.9**) that can generate both SASE FEL X-rays and incoherent radiation. An electron beam collimator was installed in front of the undulator to protect it from radiation damage by electrons with large betatron amplitudes, generated, for instance, by dark current. At FEL, off-momentum particles were a source of radiation damage to the undulator, that could not be removed in the straight collimator section. Thus, the collimator for XFEL includes a dispersive dog-leg section (**Figure 1.10**).

The European XFEL electron beam halo interaction with the collimator was simulated applying particle tracking simulation code FLUKA. In numerical calculations with FLUKA, the characteristics of geometry and materials have been taken into account.

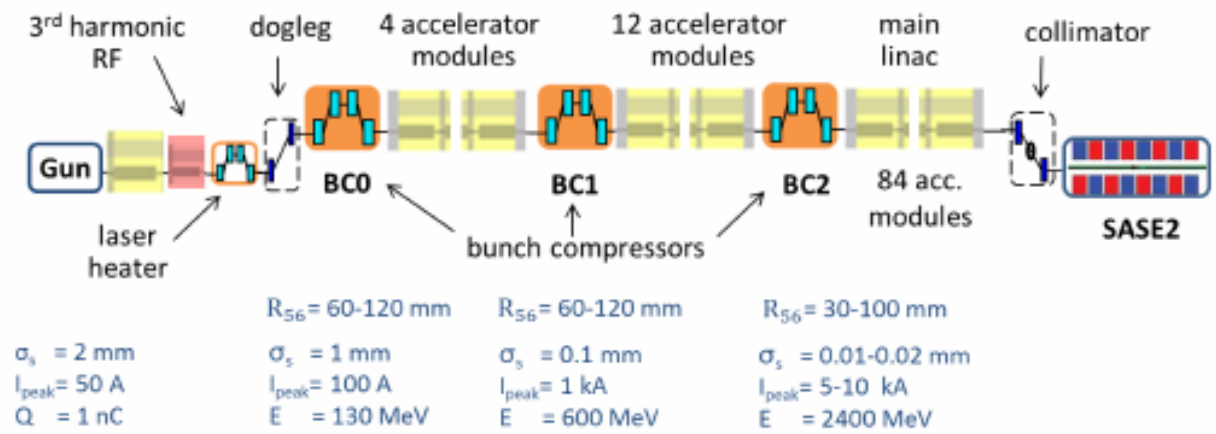

Figure 1.9: Schematic layout of the European XFEL accelerator providing electrons up to 17.5 GeV electron energy

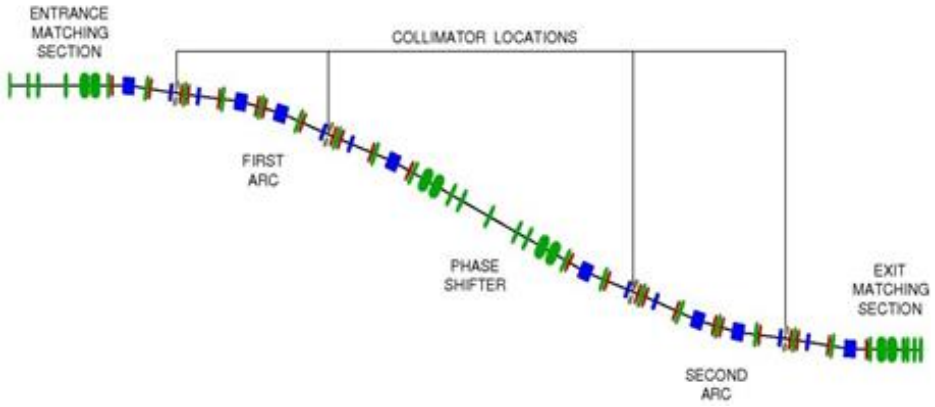

Figure 1.10: Side view of the 'dog leg', where the electron beam collimators are positioned. The vertical height is about 2.5 m

We took 17.5 GeV for the beam energy and 1.4 mm-mrad for the beam normalized emittance. Beta function is nearly 220 m at the collimator. E-XFEL linear accelerator beam main parameters are specified in **Table 1.2** [1].

Table 1.2: Beam Parameters at Undulates

Energy	**17. 5 GeV**

Emittance (normalized)	$\leq 1.4\ \mathrm{mm} - \mathrm{mrad}$
Beta function	$\approx 220\ \mathrm{m}$
Spot size	$9 \cdot 10^{-5}\ \mathrm{m}$

The beam halo consists of particles per bunch with large betatron or energy amplitudes. Evaluation of the number of large-amplitude particles, which can be expected due to the scattering processes, wake-fields, and magnet nonlinearities, is a difficult task. The beam collimation systems are applied to get rid of beam halo. The description of collimators with the picture of general view and the photo of “Collimators Block” unit is provided by Nina Golubeva [45]. The XFEL main collimator CL.COLM (4 collimators) is a system consisting of 4 Titanium alloy tubes (diameters are 4, 6, 8 and 20 mm) distributed vertically, internal pure Al block and outer Copper block (length=50cm) with brazed cooling tubes[18]. The collimator with its movers will be located inside the steel housing (length=1m), in the vacuum. In numerical calculations with FLUKA, only the main characteristics of geometry have been taken into account.

Therefore, somewhat simplified geometry was used in calculations, which includes only the main collimator block, steel housing and beam pipe (with 40.5mm diameter). The thickness of the titanium tubes and beam pipe wall is 2 mm. All tubes (0.5m long) are not tapered. Vertical direction movers enable the usage of any of four aperture of the collimator. The general view does not correspond to the exact final design **Figure 1.11**.

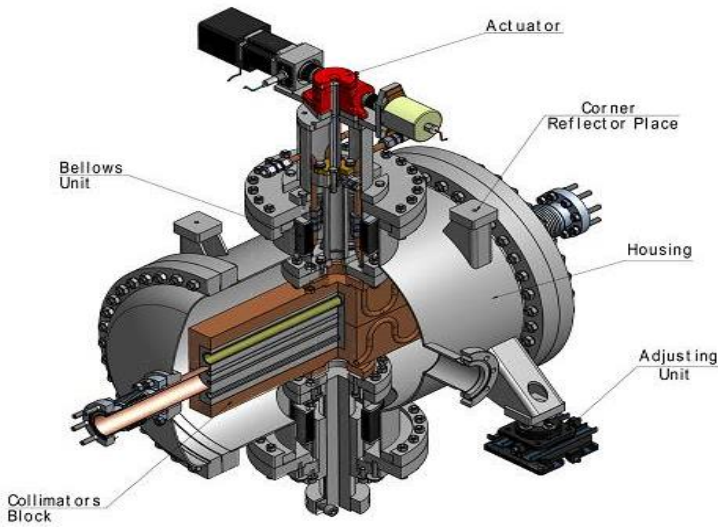

Figure 1.11: Collimator general view and photo of “Collimators Block” unit

1.14 Beam Impact on Collimator Wall

Bending or corrector magnets supply current values deviations from the stationary ones deflecting the beam to the collimator wall. The simulation of the beam impact on the collimator is important from the radiation protection point of view since a high rate of the radiation produced can be harmful both for humans and for sensitive equipment. Spatial distribution of the radiation field downstream collimator may indicate where an additional shielding would be useful. We assume that miss-stirred beam hits the front wall of the titanium tube at the coordinates x=0, y=0.4 cm. Electromagnetic cascade has been developed in the body of the titanium tube, and then the shower spreads out to the neighbouring volumes (**Figure 1.12**). All the plots shown in **Figures 1.12** and **1.13** are normalized to one of the primary particles. One can see that downstream to collimator outside beam pipe dose rate (Dose-Equivalent) reaches to a few Pico Sievert (≤10 pSv) per primary electron. That corresponds to 0.06 Sieverts per 1nC. Plots in **Figure 1.12** (right column) depict dose distribution [pSv] along the channel with maximum value. A full-scale electromagnetic shower development starts at the middle of the collimator. **Figure 1.13** shows particle fluencies from the downstream surface of the collimator [$GeV^{-1}\ cm^{-2}$]. Note that the Fluence from the surface of the housing flange prevails in the low energy region while at higher energies most radiation passes through the beam pipe cross-sectional area.

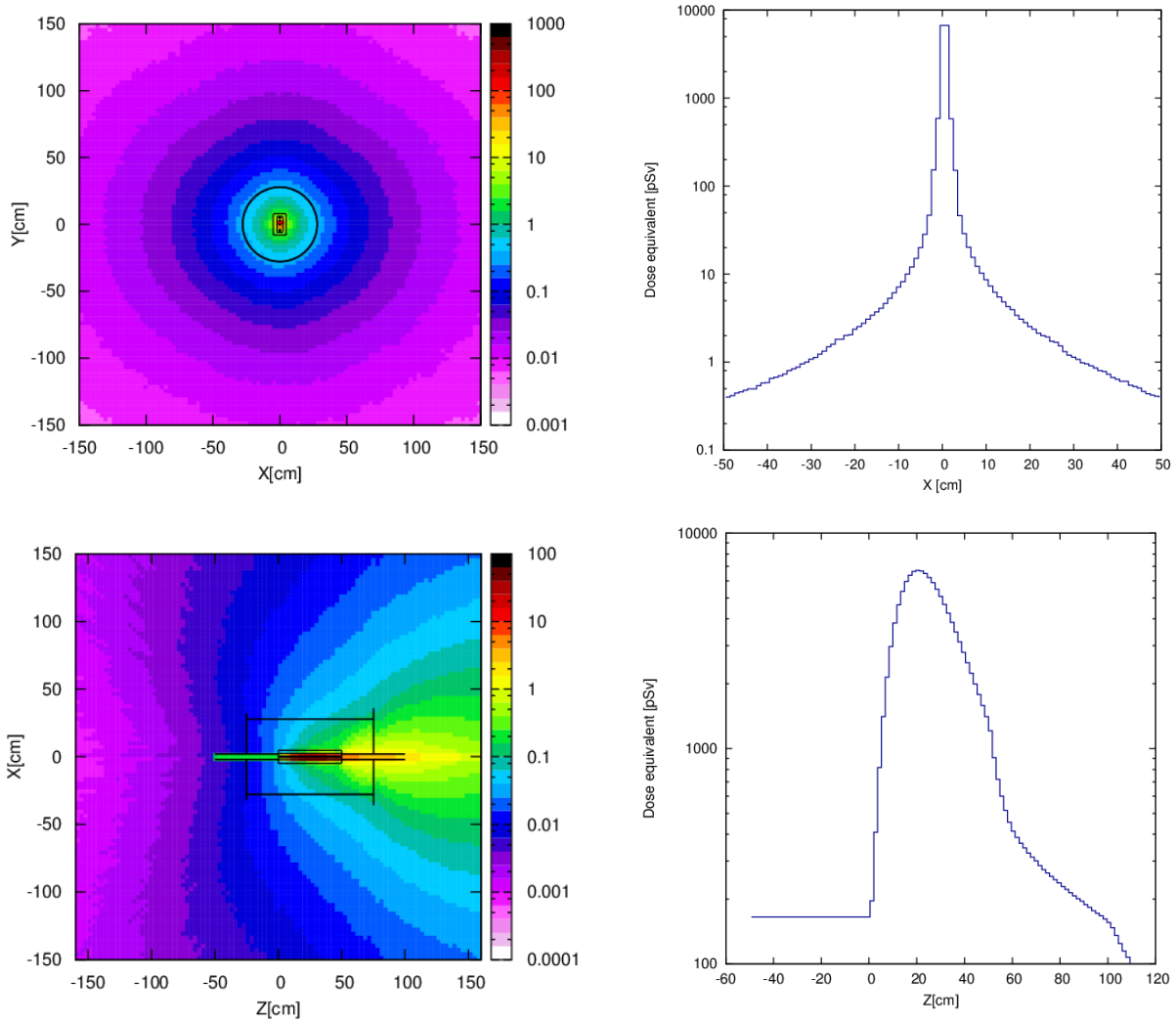

Figure 1.12: Dose distribution in picoSieverts (left column). Dose distribution in pico Sieverts along the channel with the maximum value (right column).

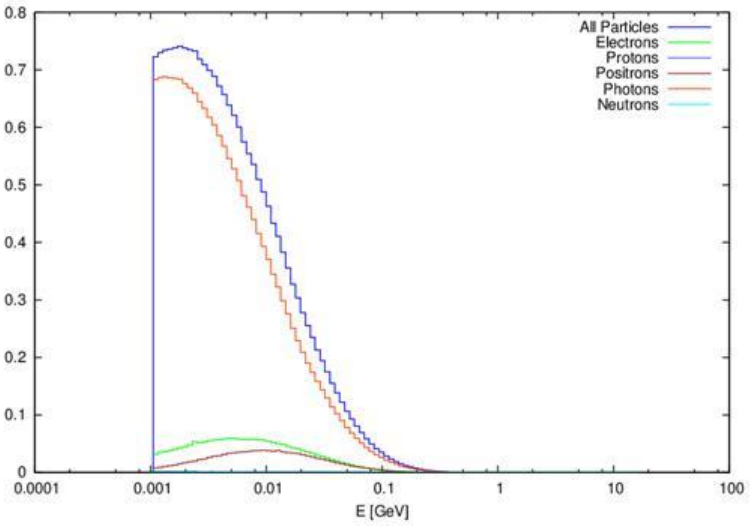

Figure 1.13: Particle fluencies from the downstream surface of the collimator [GeV^{-1} cm^{-2}].

Beam electrons lose their energy in the volume of the collimator mainly though electromagnetic showers (~75.6%), (**Table 1.3**). Hadron and muon energy loss channels compose only 0.1 % of the total energy loss. Unwanted hazardous radiation accounts for 24% of incident beam energy carried by the particles escaping the collimator.

Table 1.3: The energy available per beam particle in GeV and percentage of total energy loss is divided into several prompt radiation channels.

	GeV	**Percent**
Hadron and muon energy loss	$2.5 \cdot 10^{-2}$	0.1
Electromagnetic showers	1.32	75.6
Nuclear recoils and fragments	$1.3 \cdot 10^{-3}$	0.0
Low energy neutrons	$4.6 \cdot 10^{-4}$	0.0
Particles escaping the system	4.20	24

1.15 Beam Halo Interaction with Collimator

When radiation detectors indicate that the electron beam hits the collimator wall, the beam will be steered to the dump quickly enough to avoid significant damage by the

radiation. Thus, that mechanism cannot be considered as a halo source. Besides, the produced particles are widely spread over energy, spatial and angular ranges and the magnetic lattice will draw them promptly out of the beam orbit.

The peripherals of the beam stars just from the beam gun and a part of it passes through the magnetic lattice and reaches undulators. The particles of the beam halo are being lost continuously in interactions with the beam pipe walls. The most efficient way to get rid of the beam halo is collimation. In the result of the halo particles' impacts on the collimator walls, secondary particles coming out of collimator volume are being produced (Photons, electrons, positrons, neutrons, etc.). The dominating component of the secondary radiation is the gamma component. They are insensitive to the magnetic field of lattice and keep their direction of the motion becoming part of the general radiation background. Part of the electrons can contribute to the beam halo.

Since some processes (energy spread, lattice imperfections, interaction with the beam diagnostic equipment, various types of beam instabilities. etc.) contribute to the beam halo continuously, further collimation is necessary. Therefore, four collimators of the same type will be installed in EXFEL collimator section.

To make use of beam transport codes or just lattice transfer matrices it is convenient to rely on the FLUKA capabilities to take beam input and output files as an ASCII table with the particle parameters presented in the separate columns.

1.16 Input and Output Files Description

To make use of beam transport codes or just lattice transfer matrices it is convenient to rely on the FLUKA capabilities to take beam input and output files as an ASCII table with the particle parameters presented in the separate columns.

In order to do the calculation from the custom beam distribution, the user should be given the ASCII file. A layout of the data is organized as a table with 9 columns (ID $\mathrm{X}, \mathrm{Y}, \mathrm{Z}, \cos \mathrm{X}, \cos \mathrm{Y}, \mathrm{Cos}\ \mathrm{Z}, \mathrm{E}$), where ID is a type of particle (for example 3 for electrons), $(\mathrm{X}, \mathrm{Y}, \mathrm{Z})$ are coordinates in [cm], $(\cos \mathrm{X}, \cos \mathrm{Y}, \mathrm{Cos}\ \mathrm{Z})$ are the cosines of moving direction

with respect to axes and E is the energy in GeV. It is possible to give input file with the mixture of different particles using IDs of particles.

Output files are given the same format as input files and are written to the different files depending on particle types. For electrons, positrons, protons, photons, neutrons individual output files are created and data of other particles are written in the same files as the mixture of particles. The program is flexible enough to give output files with different formats and any customization is possible if desired. Data organization in that format makes it possible to use transfer matrices from the magnetic lattice description to transport beam parameters between the individual collimators.

1.17 Initial Halo Types

Two options of the beam halo particles spatial distribution inside beam pipe have been considered:

1) Particles are normally distributed along a radial direction with the maximum at the beam pipe axis
2) Particles' distances from the beam pipe axis are uniformly distributed

Divergence angles are chosen to be correlated with particle distance from the axis, in a way that $xx' \sim \varepsilon$, where $\varepsilon = 0.41 \cdot 10^{-10}$ is the beam natural emittance.

1.18 Halo at the First Collimator Exit

Beam halo particles spatial distribution at the entrance and exit of the first collimator is presented in **Figure 1.14 (a, b)**.

When the beam halo consisting of the normally distributed within the inner area of the beam pipe interacts with the first collimator, the halo coming out from downstream surface of the collimator in the beam pipe region is dominated by the photons (**Figure 1.15**). The majority of the electrons and positrons have the energy close to core value 17.5 GeVare being driven by the magnetic lattice to the 2nd collimator entrance while almost all photons are being lost because of the dogleg shape of the undulator section.

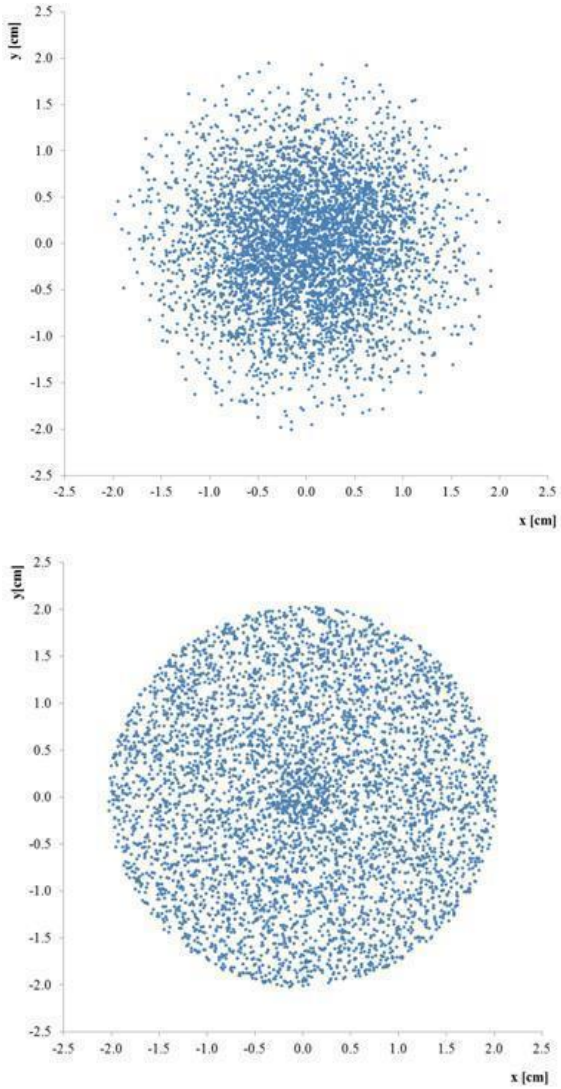

Figure 1.14a: Type 1 (Particles are normally distributed along beam pipe diameter) beam halo electrons spatial distribution at the entrance (top) and exit (bottom) of the first collimator.

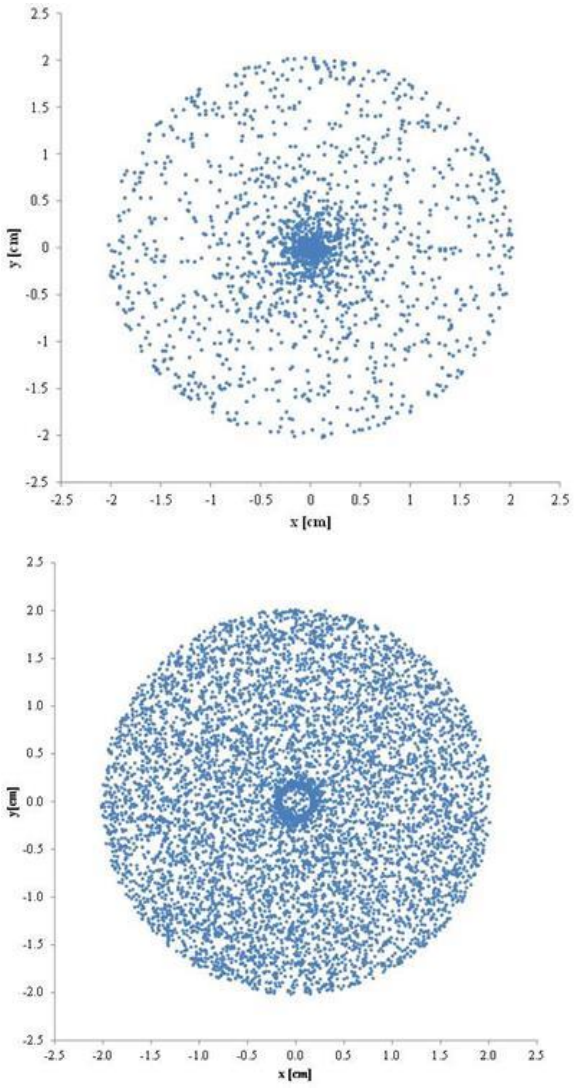

Figure 1.14b: Type 2 (Particles distances from the beam pipe axis are uniformly distributed) beam halo electrons spatial distribution at the entrance (top) and exit (bottom) of the first collimator.

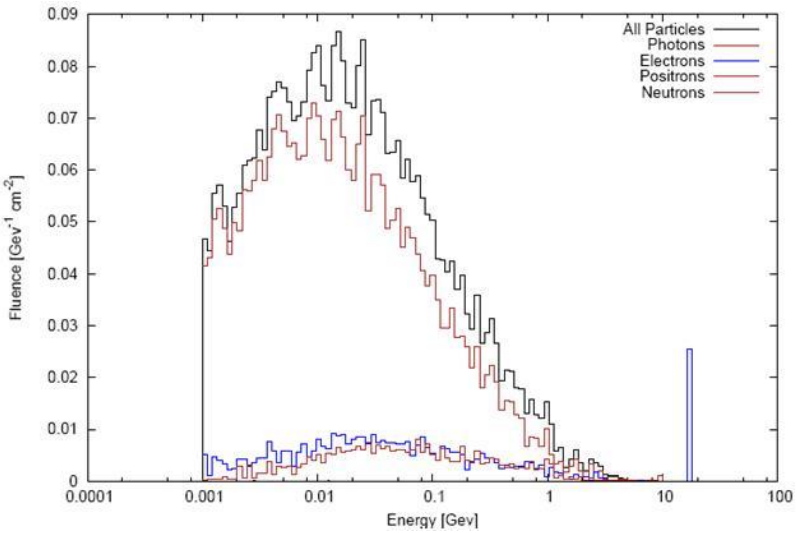

Figure 1.15: Particle fluencies from the beam pipe region of the 1st collimator surface (Particles per primary electron) produced by the beam halo.

FLUKA simulations show that the interaction of the beam halo with the first two collimators significantly reduces halo population (**Tables 1.4, 1.5**). If one assumes that halo particles mean energy is about 17.5 GeV, then 43% of halo energy is absorbed in the first collimator volume, while the mean energy of halo particles incident on the second collimator becomes 1.2 GeV, 24% of which is being lost there.

Table 1.4: Particle fluencies from the beam pipe region of the collimator surface (Particles per cm^2 per primary electron). Surface area is $12.87\ \mathrm{cm}^2$

Particle Type	**Collimator 1**	**Collimator 2**
All Particles	0.38	0.21
Electrons	$4.06 \cdot 10^{-2}$	$2.31 \cdot 10^{-2}$
Positron	$2.8 \cdot 10^{-2}$	$1.57 \cdot 10^{-2}$
Photon	0.31	0.177
Neutrons	$1.7 \cdot 10^{-5}$	$1.77 \cdot 10^{-7}$

Table 1.5: Particle fluencies from the collimator-housing surface (Particles per cm^2 per primary electron). Surface area is $50265.48\ \mathrm{cm}^2$

Particle Type	Collimator 1	Collimator 2
All Particles	11.57	6.59
Electrons	1.21	0.70
Positron	0.81	0.47
Photons	9.54	5.41
Neutrons	$5.63 \cdot 10^{-3}$	$2.26 \cdot 10^{-4}$

1.19 Interaction of the Halo with the Collimators of Four Different Apertures

To find the effectiveness of the collimator in reducing a beam halo the simulation results of the interaction of the two different types of halo with the collimators of four apertures were compared. Halo particles with energy nearly 17.5 GeV lose their energy in prompt radiation when they hit the collimator walls (**Table 1.6**). For the chosen types of the halo from ~50% (for 4mm acceptance) to ~25% (for 20mm acceptance) of the halo has been eliminated by the first collimator.

Table 1.6: The energy available per beam particle in GeV and percentage of total energy loss is divided into several prompt radiation channels

	4 mm	6 mm	8 mm	20 mm
Hadron and muon energy loss	$1.39 \times 10^{-2}(0.1\%)$	1.4×10^{-2} (0.1%)	1.2×10^{-2} (0.1%)	$7.8 \times 10^{-3}(0\%)$
Electro-magnetic showers	7.9 (45%)	7.17 (41%)	6.6 (38%)	4.44 (25%)
Particles escaping the system	9.55 (54%)	10.3 (59%)	10.9 (62%)	13.0 (75%)
Energy per beam particle	17.5 (100%)	17.5 (100%)	17.5 (100%)	17.5 (100%)

1.20 Residual Radiation Dose Calculation

Radionuclides are being produced through photonuclear and electronuclear interactions of the halo particles with collimator material. They produce residual radiation when beam operation has been stopped. The residual radiation dose has been calculated for various exposure and decay time intervals. Hadron and muon energy loss mechanism counts for only ≤0.1% of total energy loss for the particles hitting the collimator wall even for the collimator of the smallest acceptance. However, the concentration of the radionuclides will build up, causing significant slowly decaying residual radiation (**Table 1.7**, **Figure1.16**).

Table 1.7: Maximal residual dose (in Nano Sieverts) after 1000 second of beam operation for the various cooling times

Cooling time [sec.]	4 mm	6 mm	8 mm	20 mm
1	107	104	121	70.0
10	54.8	45.8	53.9	50.1
100	24.8	26.6	36.3	28.8
1000	8.6	9.6	12.7	8.9

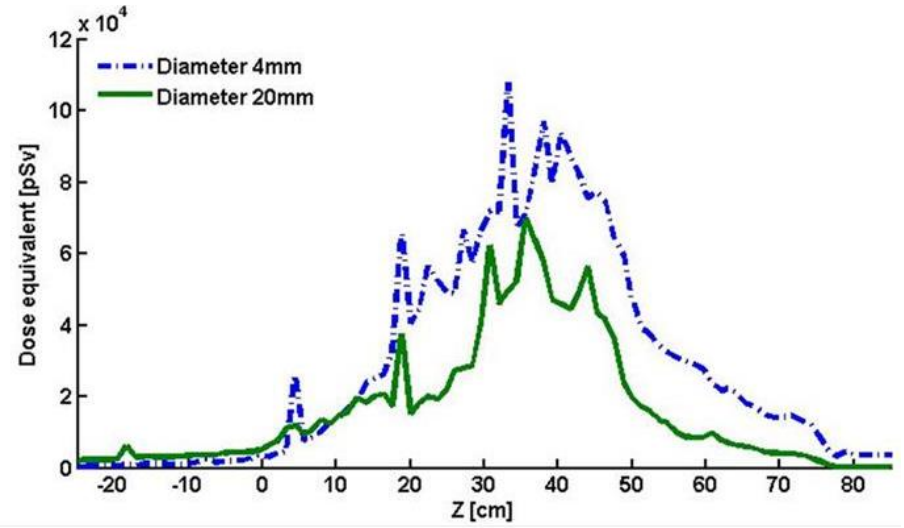

Figure 1.16: Residual dose (per primary) distribution along collimator axis for 2 values of collimator acceptance. The exposure time is 1000 sec. and the cooling time is 1 sec.

1.21 The Particle Content of the Secondary Radiation and Collimated Beam Halo

The particle content of the secondary radiation coming out of the collimator unit has been calculated (**Table 1.8**). It has been found out that the main component of the secondary radiation were photons that could not be driven by magnetic lattice field into the aperture of the next collimator were being eliminated by beam pipe walls.

Table 1.8: The energy available per beam halo particle in GeV at the exit of the collimator

	4 mm	**6 mm**	**8 mm**	**20 mm**
Electrons	5.18	6.41	7.30	10.8
Positrons	0.588	0.65	0.431	0.278
Photons	2.51	2.24	2.05	1.19
Electro-magnetic showers	7.9	7.17	6.6	4.44

1.22 Conclusion

Using particle tracking simulation code FLUKA, the European XFEL electron beam, as well as the beam halo interaction with the collimator,were simulated. The XFEL main collimator CL.COLM (4 collimators) is a system of four collimators inserted into the dogleg shape collimator section. In numerical calculation with FLUKA, the characteristics of geometry have been taken into account using SIMPLE GEO package.

We took 17.5 GeV for the beam energy and 1.4 mm-mrad for the beam normalized emittance. Beta function is $\approx 220\mathrm{m}$ (Spot size $\sigma_x$is $9 \cdot 10^{-5}$) at the collimator. The beam

halo consists of particles per bunch with large betatron or energy amplitudes. Two types of beam halo filling the inner volume of the beam pipe were simulated.

Bending or corrector magnets supply current values deviations from the stationary ones, which can deflect the beam to the collimator wall. The simulation of the beam impact on the collimator wall is important from the radiation protection point of view since the high rate of the radiation produced can be harmful both for humans and for sensitive equipment. The results of the simulation of the beam impact on the collimator wall show that downstream to collimator outside beam pipe dose rate (Dose-Equivalent) reaches to a few Pico Sieverts (≤ 10 pSv) per primary electron.

To find the effectiveness of the collimator in reducing a beam halo the interactions of the two different types of halo with the collimator were simulated. The parameters of the electrons coming out from the downstream surface of the collimator were transferred to the entrance of the next collimator at the EXFEL collimator section using linear transfer matrices.

The study of the beam halo dynamics is in progress including the evaluation of the number of large-amplitude particles, which can be expected due to the scattering processes, wake-fields, and magnet nonlinearities.

1.23 Flash Tapered Collimator

FLASH has been an FEL user facility since 2005 which can produce XUV and soft X-ray radiation in the wavelength range from 4.1nm to 45nm (**Figure 1.17**). Collimators are used in FLASH and European XFEL to cut off electron beam halo [1-2]. We will use FLUKA [52] to simulate the interaction of the electron beam with the FLASH and European XFEL collimators made of Titanium and Copper. The main characteristics of the collimator materials are given in **Table 1.9**.

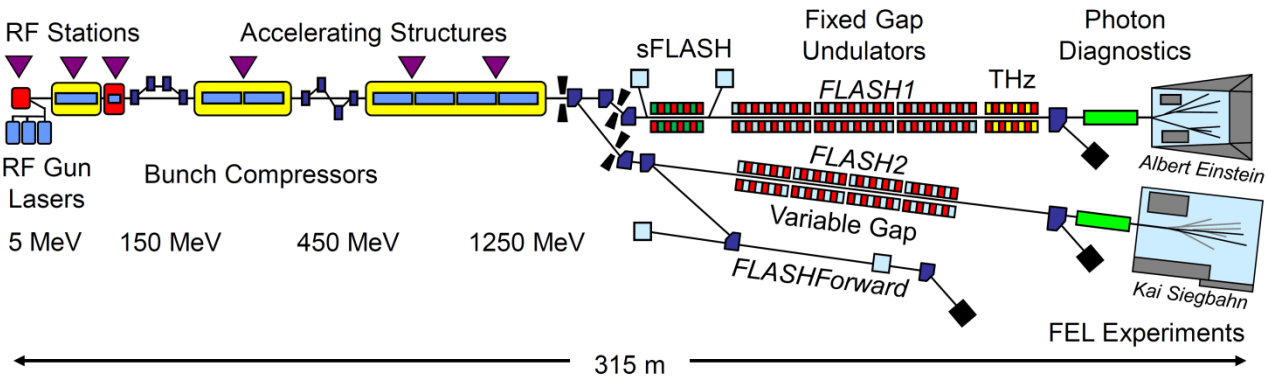

Figure 1.17: Schematic layout of FLASH facility.

Table 1.9: Collimator Material Properties

Property	Copper	Titanium
Z	29	22
A	63.55	47.88
Density [g/cm^3]	8.96	4.54
Radiation length [cm]	1.43	3.56
Moliere radius [cm]	1.6	2.85
Critical energy [MeV]	20.2	26.3

On FLASH facility four cylindrical symmetric copper made tapered collimators of the same type are installed [67]. The collimators are cylindrical tubes with inner tapered holes. The geometry of collimators is similar to **Figure 1.18** with the length of the tapered parts is $L_1 = 200\,mm$ each and non-tapered central part length is $L_2 = 100\,mm$. Minimal inner radius is $b = 0.2\,mm$, while maximal inner radius at the ends is equal to $d = 4.5\,mm$. The collimator is made up of copper with a conductivity of $k = 5.8 \times 10^7\,S/m$.

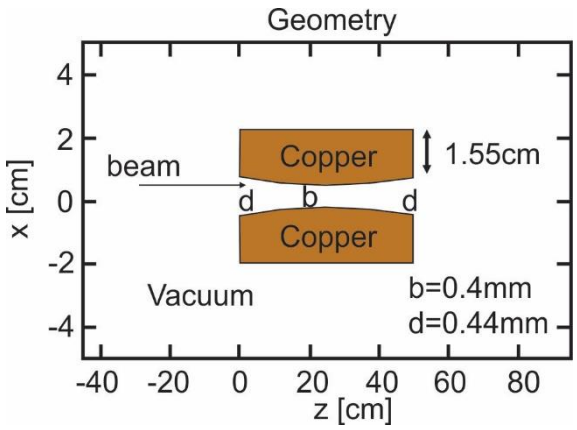

Figure 1.18: FLASH Tapered Collimator cross-Section.

It is assumed that FLASH 1.27 GeV beam electrons hit collimator inner wall at a grazing angle on the XZ plain (**Figures 1.18**). Energy deposition in the collimator volume and its vicinity is calculated using FLUKA, which allows simulating energy deposition or particle fluence on the given mesh independent of the geometry. Plots are normalized to 1nC primary charge.

Absorbed dose distribution XY projection is shown in **Figure 1.19**. Absorbed dose is expressed in Greys (J/kg). Within the hole of the collimator, where the material does not exist (vacuum), absorbed dose is zero. The maximal dose can be found near the beam impact point. Absorbed dose distribution XZ projection is shown in **Figure 1.20**. Absorbed dose is expressed in Greys (J/kg). Distribution maximum is shifted towards positive X direction coinciding with the beam impact point. Radiation dose distribution XY projection is completely symmetric with respect to Y-axis.

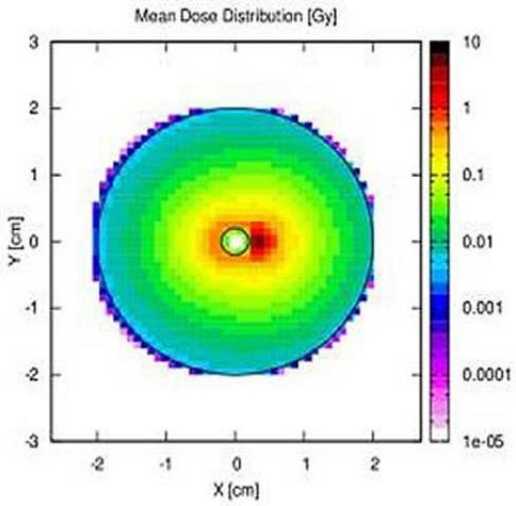

Figure 1.19: Energy deposition distribution in the collimator material in the XY plain

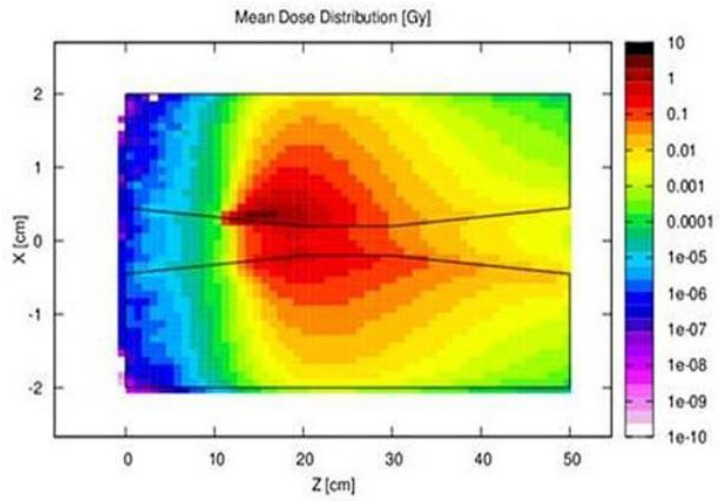

Figure 1.20: Energy deposition distribution in the collimator material in the XZ plain(absorbed dose in Greys).

The main component of the radiation is the photon component. Based on the absorbed dose distribution YZ projection depicted in **Figure 1.19** one can conclude that the most radiation is emitted towards the upstream direction. In the downstream direction, radiation is effectively being absorbed by collimator material and much less amount of the radiation leaves collimator body. Another important component of the radiation is neutron radiation. Though neutrons carry much less energy compared to gamma component, they have a high penetrating capacity. As compared to photons, a larger part of neutrons penetrates collimator body in the downstream direction.

Beam particles incident on collimator loses 84% of their energy via electromagnetic shower while secondary radiation particles leaving collimator material carry 16% of energy (**Table 1.10**).

Table 1.10: The energy available per beam particle in GeV (% of total energy loss) is divided into prompt radiation channels

Property	EXFEL titanium collimator	EXFEL copper absorber	FLASH tapered collimator
Hadron and muon energy loss	0.012 (0.1%)	$1.0 \cdot 10^{-4}$ (0.0%)	$9.5 \cdot 10^{-4}$ (0.1%)
Electro-magnetic showers	11.6 (70.4%)	$3.8 \cdot 10^{-2}$ (0.2%)	1.1 (84%)
Nuclear recoils and fragments	$5.9 \cdot 10^{-4}$ (0.0%)	$7.0 \cdot 10^{-6}$ (0.0%)	$3.7 \cdot 10^{-5}$ (0.0%)
Low energy neutrons	8.9 $\cdot 10^{-5}(0.0\%)$	$9.0 \cdot 10^{-8}$ (0.0%)	$1.1 \cdot 10^{-5}$ (0.0%)
Particles escaping the system	4.84 (29.3%)	16.46 (99.8%)	0.2 (16%)
Energy per beam particle	16.5 (100%)	16.5 (100%)	1.27 (100%)

Maximal dose distribution along three Cartesian coordinate axes revel the following: a) X-distribution has a maximum at small X values corresponding to the position of the point where beam hits the collimator inner wall; b) Y distribution is symmetric with respect to X axis **Figure 1.21.**

The peak of X-distribution of the maximal dose (dose in bin, where dose is maximal) is shifted towards positive X direction.

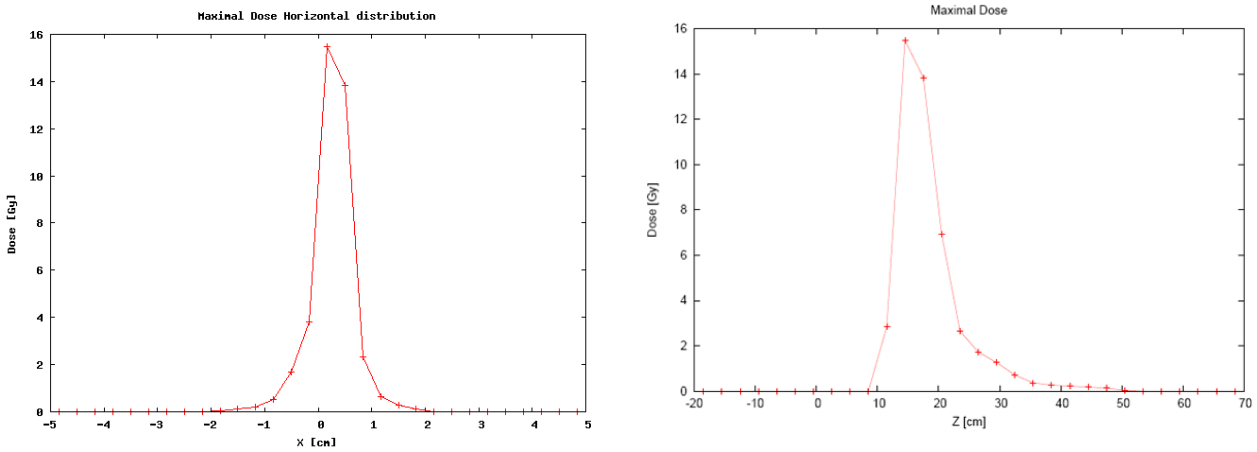

Figure 1.21 Energy deposition (absorbed dose in Greys) a) vertical distribution in the collimator material,b) along beam axis in the collimator material.

FLUKA USRTRACK card scores average $d\Phi/dE$ (differential fluence)of a given type or family of particles (or energy) in a given region **Figure 1.22.**

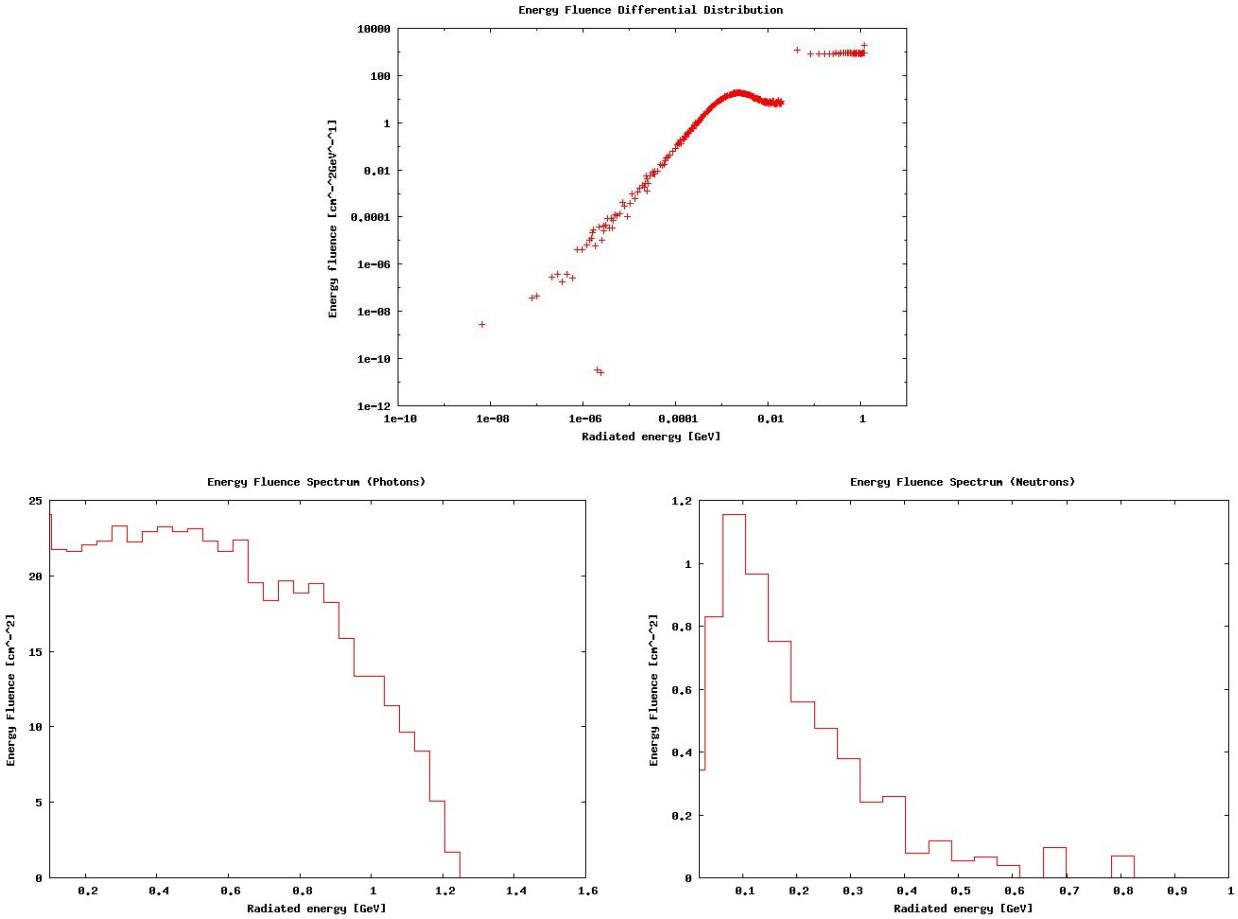

Figure 1.22. Differential fluence of radiated energy in a collimator estimated by FLUKA USRTRACK card.

1.24 XFEL Cylindrical Step Collimator

On XFEL facility cylindrical symmetric titanium made collimator is installed [54]. The length is 500 mm, the inner radius is 2 mm, while the outer one is 20 mm. The collimator is made of titanium with material parameters presented in **Table 1.9**. It is assumed that the European XFEL 16.5 GeV beam electrons hit collimator front wall.

Beam particle incident on collimator losses 70% of its energy via electromagnetic shower while secondary radiation particles leaving collimator material to carry 29% of energy (**Table 1.10**). Radionuclides are being produced via photonuclear and electro nuclear interactions, thus causing residual radiation when beam operation has stopped (**Figure 1.23** and **Table 1.11**). It should be noted that a given amount of radionuclides are being produced if beam bombards the collimator body for two weeks. It will take much longer time to get a significant amount of the radionuclides if only beam halo particles hit the collimator.

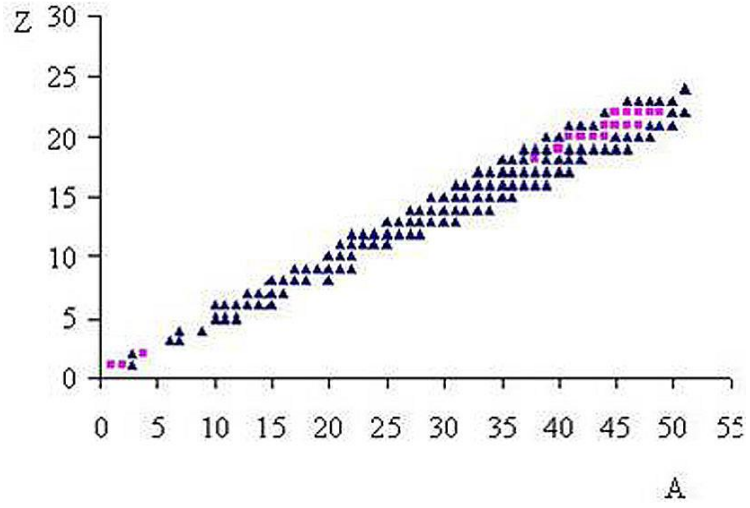

Figure 1.23: Produced residual nuclei within the titanium collimator body after 2 weeks beam operation. Triangles denote the nuclei with the yield greater than 10^{-6} nuclei/cm^3/pr while squares denote the nuclei with the yield greater than 10^{-2} nuclei/cm^3/pr.

Table 1.11: Residual Nuclei with the Yield Greater than 0.1nuclei/cm^3/Primary

Nuclides	Yield[nuclei/cm^3/pr]
^{1}H	0.5331
^{4}Be	0.1569
^{46}Ti	0.3326
^{47}Ti	0.9713
^{48}Ti	0.2848

1.25 XFEL Undulator Intersection Tapered Collimator

On XFEL facility undulator intersections cylindrical symmetric copper made tapered collimators are installed [67]. The geometry of collimators is similar to that of **Figure 1.19** and **Figure 1.20** with the length of the tapered parts $\mathrm{L}_1 = 9.5\ \mathrm{mm}$ each and non-tapered central part length $\mathrm{L}_1 = 3$. Minimal inner radius is $\mathrm{b} = 0.4\ \mathrm{mm}$, while maximal inner radius at the ends is equal to $\mathrm{d} = 0.44\ \mathrm{mm}$.

Beam particle incident on collimator losses only 0.2% of its energy via electromagnetic shower while secondary radiation particles leaving collimator material carry 99.8% of energy (**Table 1.10**). **Table 1.12** presents the composition of the radiation from the surface of the copper absorber.

Table 1.12: Composition of the Radiation from the Surface of the Copper Absorber

Particles	Particles per primary
Electrons	$4.64 \pm 0.08\%$
Positrons	$2.42 \pm 0.26\%$
Protons	$4.06 \pm 4.0\%$
Neutrons	$0.026 \pm 2.6\%$
γ-Quanta	$18.7 \pm 0.01\%$
Total	$25.8 \pm 0.07\%$

1.26 Conclusion

The European XFEL electron beam interaction with the titanium collimator and copper absorber of the undulator intersections, as well as FLASH beam interaction with the tapered collimator, were simulated applying particle tracking simulation code FLUKA. Absorbed dose spatial distribution in the material of the collimators was simulated for the total secondary radiation and its most important gamma and neutron components. The energy spectrum of the produced total radiation and its photon and neutron components were calculated. Angular and spectral double differential distributions of the radiation energy emitted by collimator surfaces were obtained. Residual dose rate after irritation of the collimator material by the electron beam was calculated. Particle fluencies from the collimators surface (particles per primary electron) are presented in **Table 1.13**.

The obtained outcomes can be used to assess the effectiveness of the collimators for eliminating beam halo and make a decision on radiation protection measures. A detailed study of the secondary radiation composition, spectrum, dose, angular and spatial distribution by means of particle tracking simulation is on the way.

Table 1.13: Particle Fluencies from the collimator surface (particles per primary electron)

Collimator	Total	Photons	Neutrons
EXFEL titanium collimator	$14.0 \pm 0.032\%$	$12.0 \pm 0.024\%$	$0.03 \pm 0.49\%$
EXFEL copper absorber	$25.8 \pm 0.069\%$	$18.7 \pm 0.084\%$	$0.026 \pm 2.6\%$
FLASH tapered collimator	$0.408 \pm 0.05\%$	$0.375 \pm 0.043\%$	$0.0015 \pm 2.4\%$

SUMMARY

- The European XFEL electron beam interaction with the complex shape collimators and copper absorbers in the undulator intersections as well as FLASH FEL beam interaction with the tapered collimator were simulated applying particle tracking simulation code FLUKA.
- The simulations results indicate that two collimators (out of 4 installed) are enough to get rid of the halo entering the collimator section effectively.
- The results of the simulations of the beam impact on the collimator wall show that downstream to single collimator outside beam pipe dose rate (Dose-Equivalent) reaches to a few Pico Sieverts (≤10 pSv) per primary electron.
- The results of digital simulations of the FLASH FEL beam interaction with the tapered collimator yield data that have been useful for efforts toward the minimization of the degradation effect of radiation on the undulator permanent magnet blocks.

Chapter 2: Radiation Safety Considerations for AREAL Electron Linac

2.1 Introduction

The AREAL linear accelerator will produce an electron beam with 5 MeV energy and further upgrade up to 20 MeV. At the first stage of the operation, the construction of the beam diagnostic section of complex shape and layout is planned, thus making the radiation source definition difficult. Further, when AREAL construction was finished and machine running was launched successfully it gave an opportunity to compare simulation results with experiments. Comparison of experimental data with simulations is performed with the combination of theoretical models. FLUKA particle tracking simulation code was used to calculate the produced radiation dose rated, and define an appropriate radiation shielding. All physical objects which could impact the radiation fields such as magnets, electric field, and obstacles in the path of the beam were taken into account based on the real geometrical setup of the machine.

The purpose of this study is to determine the radiation dose at linear accelerator AREAL (3.7 MeV) facility and compare simulation results with experimental measurements. The characteristics of geometry have been taken into account. The FLUKA particle tracking simulation code was used to simulate radiation dose of the electron beam with 3.7MeV energy. For the linear accelerator AREAL, custom programs (using FORTRAN) called “routines” were developed to improve the simulation results. The custom routines were programmed to define the 3D magnetic field in FLUKA, output beam parameters and input parameters of the primary electron beam respectively. Comparing simulation results with data measured in experiment via Faraday Cup (which measures beam charge), YAG screen (which measures beam profile) and dosimeter is possible only by using custom routines.

The development of the modern large-scale projects of X-ray Free Electron Lasers (FEL) like FLASH, European XFEL and LCLS, which put stringent conditions on electron beam quality, was probably the main reason bringing the laser-driven photo-

electronic RF guns into the focus of scientific research since they allow the generation of short electron bunches with low emittances suitable for the injection into low emittance linear accelerators [1,68, 69]. The Photo Injector Test Facility (PITZ) at the DESY was created aiming at testing and optimization of the sources of high brightness electron beams for future free electron lasers and linear colliders [70]. REGAE the Relativistic Electron Gun for Atomic Exploration is another small electron accelerator build and at DESY in order to provide high-quality electron bunches for time-resolved diffraction experiments, and serves as a test facility for accelerator research. The AREAL linear accelerator is designed to provide ultra-short electron pulses with small emittance [71]. The photo-electronic RF gun of AREAL produces an electron beam with the energy of 2-5MeV and bunch charge of 10-250pC that is being used for the several material and life science irradiation experiments [16,72] along with accelerator and particles beam physics research. The secondary radiation has been generated when the electron beam interacts with the material on the beam trajectory (beam dump target, beam pipe walls, detectors and beam diagnostic equipment). In the current study low energy electron beam interaction with matter has been investigated applying both numerical simulation and experimental measurement methods. For the determination of radiation field (radiation dose and its spatial and angular distribution in the AREAL machine hall and neighbouring rooms) by computer simulation of the beam interaction with matter has been performed along with the direct measurement of the radiation dose rates. FLUKA Monte Carlo particle transport code has been used [20].

The radiation dose simulations using digital simulation computer codes are necessary for the design and development of the adequate radiation shielding and for the planning of the radiation protection measures in stages of the particle accelerator construction, operation and update. A general consensus exists, that Monte-Carlo codes, such as FLUKA, EGS4, GEANT, MCNPX, and MARS provide accurate results for shielding design purposes, in particular for complicated three-dimensional geometries [73]. The choice of the FLUKA code is based on the consideration that an operational up to date version of the code is available, and FLUKA gives an opportunity

to track the particles to the low energies consuming reasonably affordable computational resources and time.

FLUKA has been in use widely for radiation protection related research and development in the CERN, SLAC, CEBAF and other accelerator centers [14,74-75].

In the result of the primary electron beam interaction with the matter the following sources of the secondary radiation: beam dump, FC, YAG screen targets, beam-pipe walls, vacuum windows, and air have been considered during the computer modelling of the radiation field in the experimental hall of the low energy electron facility AREAL. Beam characteristics obtained by beam diagnostic measurement and hall equipment geometry have been taken into account accurately in numerical simulations based on FLUKA particle tracking code. Dose measurements by high precision ion chamber dose meter have been carried out, and satisfactory agreement between measurement results and the numerical simulation results has been found.

Since dose measurements prove the reliability of simulation results, the radiation shielding contraction design and creation, as well as the radiation safety procedures development, have been realized in a routine manner based on numerical simulation data.

Both calculation data based on numerical simulation and dose measurement proved that radiation dose levels in the AREAL machine hall and experimental rooms were under the control and conform completely to the radiation safety requirements for equipment and personnel.

2.2 Radiation levels:

- Natural background dose: On a worldwide average, the whole-body dose equivalent during a year due to all sources of natural background radiation varies from $1.0\ to\ 13\ mSv$ $(0.1–1.3\ rem)$ with an yearly average of $2.4\ mSv$ [76]. In certain geographical areas values up to $50\ mSv$ $(5\ rem)$ were detected. A large portion (typically more than 50%) is generated from inhaled natural radioactivity which produced mostly radon and radon daughters. It can vary up

to 10 times: natural background does is $0.1-0.2\ mSv$ in open areas, in a house $2\ mSv$ on average and more than $20\ mSv$ in poorly ventilated closed areas such as mines.

- Cosmic ray background dose: At the level of sea, the whole-body dose equivalent due to cosmic rays background radiation is dominated by muons and nucleons at higher altitudes. Dose equivalent rates varies from less than $0.1\ \mu Sv/h$ at level of sea to a few $\mu Sv/h$ at aircraft altitudes. Details on cosmic ray fluence levels are provided in the Cosmic Rays section.
- Recommended limits of the effective dose: The International Commission on Radiological Protection (ICRP) recommends an effective dose limit for radiation workers of $20\ mSv$ per year averaged over 5 years, with the assumuption that the dose should not exceed $50\ mSv$ in any single year [77]. Dose limit in the EU-countries and Switzerland is $20\ mSv$ per year, in the United States it is $50\ mSv/year$ ($5\ rem$ per year). Many scientific laboratories in the United States and elsewhere may set lower limits. The dose limit for general public is typically $1\ mSv$ per year.

2.3 Radiation protection instrumentation:

The capacity to differentiate and measure the high-LET (mostly neutrons) and the low-LET components (electrons, photons, muons) of the radiation field at working areas is of primary importance to evaluate the exposure of staff. At proton accelerators the prompt dose equivalent outside a shield is mainly caused by neutrons, with some contribution from gamma radiation and, to a minor extent, charged particles. Most of the staff exposure at accelerator facilities is usually received during maintenance works, and it is caused by gamma/beta radiation coming from residual radioactivity in accelerator elements.

Radiation dosimeteres used both for radiation surveys and area monitoring are usually calibrated in ambient dose equivalent $\mathrm{H}^{*}(10)$ [78].

2.4 Geiger Muller counters

Geiger Muller (GM) counters are low cost and widespread devices and simple to operate. (GM) counters work in pulse mode and since they only count radiation-induced events the spectrometric information is lost. Usually they are calibrated in units of air kerma, for instance in a $60Co$ field. The response of Geiger Muller counters to photons is consistent within 15% for energies up to $2\,MeV$ and shows significant energy dependence above[79].

2.5 Ionization chambers

Ionization chambers detectors are gas-filled and used both as hand-held instruments (e.g., for radiation surveys) and environmental monitors. They are normally operated in current mode although pulse-mode operation is also possible. They have a relatively flat response to a wide range of X- and a gamma ray energies (from $10\,keV$ to several MeV), can measure radiation over a wide intensity spectrum and are capable of individualizing between the gamma and beta components of a radiation field (by use of, e.g., a beta window). Pressurized ion chambers (e.g., with Ar or H gas to several tens of bars) are used for environmental observations. They have good responsiveness to neutrons and charged hadrons in addition to low LET radiation (muons and gammas), with the response function to the former being strongly non-linear with energy[79].

2.6 Radiation Produced by Electron Beam

Neutron and photon radiation emitting from thick samples can be grouped (roughly) into five different components:

- Giant-Resonance Neutron (GRN): Neutrons having energies in the $0.1 < E < 20MeV$ range. These are known as fast-neutrons are photo-produced in the core of the shower by mechanism known as giant-resonance excitation.
- High-Energy Neutron (HEN): Neutrons having energies above $100\,MeV$ that are an integral part of the hadronic cascade that is originated by high-energy photons in the Electro-Magentic cascade. Although the High-Energy Neutron

(HEN) component is the radiation type that dominates for thick shields (i.e., 4 or more feet of concrete), (HEN) themselves are difficult to detect experimentally. What is usually measured is evaporation neutrons ($< 20\,MeV$) generated in high-energy hadronic events (called "stars"). These low-energy neutrons are known also as the "camp followers" of the hadronic cascade.

- Mid-Energy Neutron (MID): Neutrons with energies between the GRNs and HENs ($20 < E < 100\,MeV$), including those generated by means of the quasi-deuteron reaction[80].
- Direct Gamma (GamD): Photons emitting directly from the core of the EM shower with energies varying in $0.1 < E < 20\,MeV$ range, as defined by thick-target penetration through the so-called "Compton window" (i.e., mass attenuation coefficient minimum). The angular distribution of radiation consists of a slowly decreasing level from$0^0 - 180^0$, superimposed onto which is a very forward ($0^0 - 5^0$) bremsstrahlung core [81-86].
- Indirect Gamma (GamI): Directly ionizing particles and photons (e.g., charged pions) that guide the attenuation of the High-Energy Neutron field in the shield. This radiation type has been experimentally determined to be slightly more than 25% of the HEN dose rate. Each of these radiation components can be described by an empirical model. That model is experimentally based on what we have traditionally called the standard-target arrangement—particularly, a 12-inchlong cylinder of iron, having a radius of 2-inches, that is struck by a$10\,GeV$ electron beam[87].

2.7 Gamma Shielding

Protection from gamma rays requires large amounts of mass. Gamma rays are absorbed best by materials with high atomic numbers and high density. Neither effect of those is important compared to the total mass per area in the path of the gamma ray. Because of this, a lead shield is only slightly better ($20 - 30\%$) as a gamma shield than

an equivalent mass of another shielding material such as concrete, aluminium, or soil; lead's major advantage is its high density[88].

The higher the energy of the gamma's photons, the thicker the shielding should be. Materials for protection against gamma rays are typically measured by the thickness required to reduce the intensity of the gamma rays by one-half (the 1/2 value layer so-called HVL). For example, gamma rays that need $1\ cm$ of lead to reduce their energy by 50% will also have their energy reduced in half by $6\ cm$ of concrete, $9\ cm$ of packed soil or $4.1\ cm$ of granite rock. However, the mass of this much soil or concrete is only $20-30\%$ larger than that of the lead with the same capability of absorption. Depleted uranium is used for shielding in transportable gamma ray sources, but again the savings in weight over lead is slight, and the main effect is to reduce shielding mass[89].

2.10 Health Effect

At a cellular level all ionizing radiations causes' similar damage, but because rays of beta particles and alpha particles are relatively non-penetrating, external exposure to them causes only localized damage, e.g. radiation burns to the skin[90]. Neutrons and gamma rays are more penetrating, causing diffuse damage throughout the body (e.g. radiation sickness), increasing the incidence of cancer rather than burns. External radiation exposure should also be differentiated from internal exposure, because of inhaled or ingested radioactive substances, which, depending on the substance's chemical nature, can produce both localized and diffuse internal damage. The most biological damaging forms of gamma rays occur in the gamma ray window, ranging from $3\ MeV$ up to $10\ MeV$. Higher energy gamma rays are less harmful because the body is relatively transparent to them[91].

2.11 Beam Dump

The beam dump will consist of an iron core with lateral and downstream shielding. Iron target will be $30\ cm$ long cylinder with $5\ cm$ thickness. Ten cm Led shields will

surround iron core (laterally and downstream) and $50\ cm$ thick concrete brick wall will compose outer shielding of the beam dump.

Dose produced at beam dump Standard-Target and shielding calculations are based on the algorithms and formulae contained in SHIELD11 computer code [92], as well as simulated by FLUKA particle tracking code. The angular and energy distribution of the gamma radiation emitted directly in shower core at the iron target can be expressed by the following formula [92].

$$D_\gamma = \left(\frac{EI}{q_e}\right) \times \begin{pmatrix} 3.031\, E e^{-0.959\sqrt{\vartheta}} \times 10^{-13} \\ +7.5\, e^{-\vartheta/72.2} \times 10^{-8} \end{pmatrix} \quad (2.1)$$

Here D_γ is the gamma dose rate at the radiation source in the units of $[Sv/h]$, I/q_e is the beam particles fluence (it reaches to value 1.25×10^9), E is the beam energy in $[MeV]$ s and ϑ is radiation angle in degree with respect to the beam direction. For $E = 20MeV$ and $\vartheta = 90$ degrees one gets $D_\gamma = 0.538\, Sv/h$. **Figure 2.1** illustrates direct gamma radiation, dose per electron distribution at beam dump target for $20\ MeV$ beam. Maximum of radiation lays in the forward direction and increases with electron energy nearly linearly.

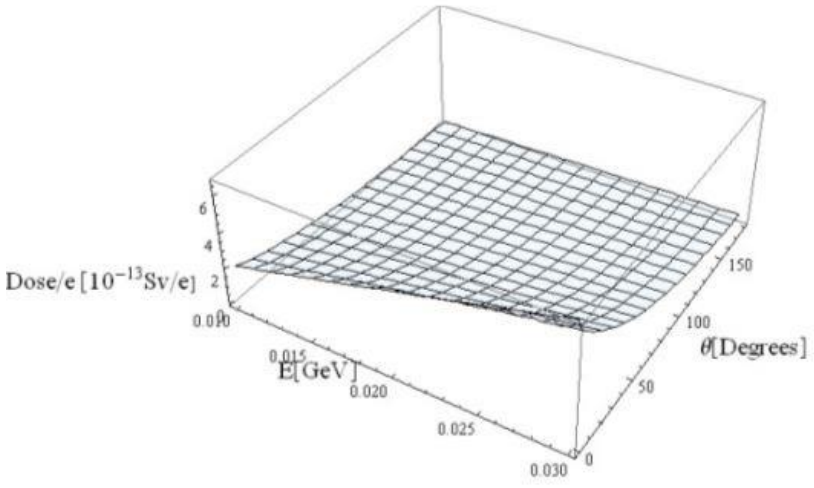

Figure 2.1: Direct gamma radiation dose per electron at the standard target

The composition of the radiation (in the units of $particles/cm^3$ per primary) produced by $20\ MeV$ electrons incident on iron target core is given in **Table 2.1**.

Table 2.1: Beam Target Radiation Composition

	Particles/cm^3/primary	**Accuracy**
Neutrons	0.0035	4.6%
Electrons	1.40	0.0019%
Photons	10.0	0.024%

The shielding has to be dimensioned to keep the ambient dose equivalent rate below the limit of 0.125 $\mu Sv/h$ (the sum of both, the neutron and γ- dose rates) [92, 93]. The parameters of some common shielding materials are given in **Table 2.2**. The mean free path $\lambda[g/cm^2]$ is the parameter that defines materials ability to absorb radiation$F = F_0 e^{-\lambda/d}$, where F is the fluence and d $[g/cm^2]$ is the material thickness. Neutrons are effectively being absorbed by concrete since it contains hydrogen (in bounded water molecules). For the attenuation of the gamma radiation high Z materials (like Led) are being applied **Table 2.2**.

Table 2.2: Density and removal free path for used shielding materials.

	Concrete	**Fe**	**Pb**
ρ $[g/cm^3]$	2.35	7.87	11.35
Neutrons $[g/cm^2], [(cm)]$	$30, (12.8)$	$47, (5.97)$	$97, (8.55)$
Gamma $[g/cm^2], ([cm])$	$42, (17.9)$	$33.6, (4.27)$	$24, (2.11)$

Figure 2.2 depicts dose outside tunnel vs. concrete shielding thickness. The dotted line shows the target level of equivalent dose ($0.125\mu Sv/h$). Additional 10 cm Led shielding around the beam dump target effectively reduces gamma dose. One should notice that concrete shielding total thickness is the sum of tunnel wall thickness and that of removable shielding wall around the radiation source.

Figure 2.3 demonstrates spatial distribution (in the plain perpendicular to the beam direction) of the Equivalent dose per electron in picoSieverts in the beam dump vicinity for 20 MeV beam energy simulated by FLUKA.

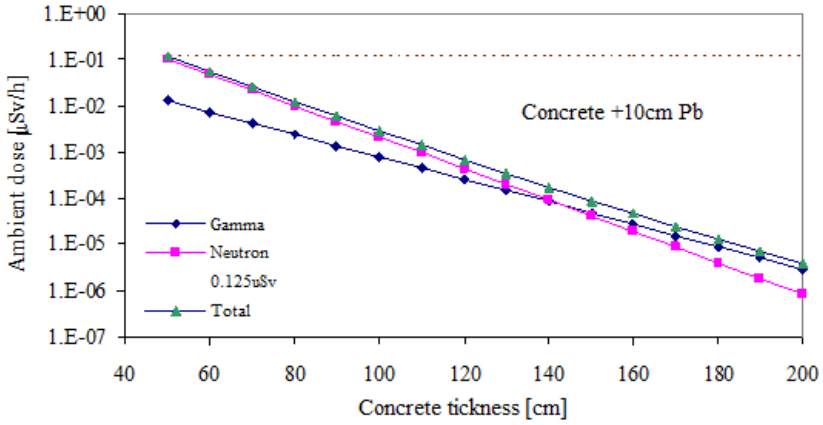

Figure 2.2: Ambient dose outside tunnel vs. concrete shielding thickness. Dotted line shows target level of equivalent dose.

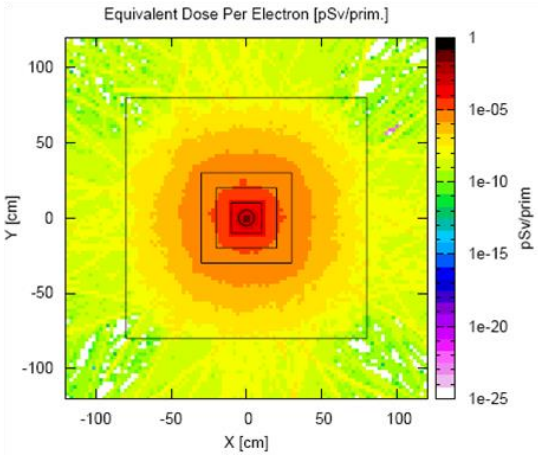

Figure 2.3: Equivalent dose per electron in picoSieverts in the beam dump vicinity for 20 MeV beam energy (FLUKA simulation).

2.12 Radiation from Beam Diagnostic Equipment

At the AREAL linac, Faraday Cups will be inserted into the electron beam path to measure the beam charge. Faraday Cup is made of stainless steel and will collect the complete charge of the train of the $200\,pC$ bunches becoming the source of the secondary radiation. A DC voltage is applied to reduce the number of electrons leaving

the surface so that the emitted radiation almost completely consists of gamma quanta. $YAG:Ce$ scintillation screens will be used for the beam profile measurements.

Radiation sources related to beam diagnostic system (**Figure2.4**) are the followings:

- Faraday Cup for beam current measurement at the end of arc section
- Faraday Cup for beam current measurement at end of “pepper pot”
- Scintillation screen for the beam profile measurements
- Scintillation screen for the beam energy and energy profile measurements
- “Pepper pot” Tungsten mask for beam emittance measurements
- Beam chamber walls at the bending magnet

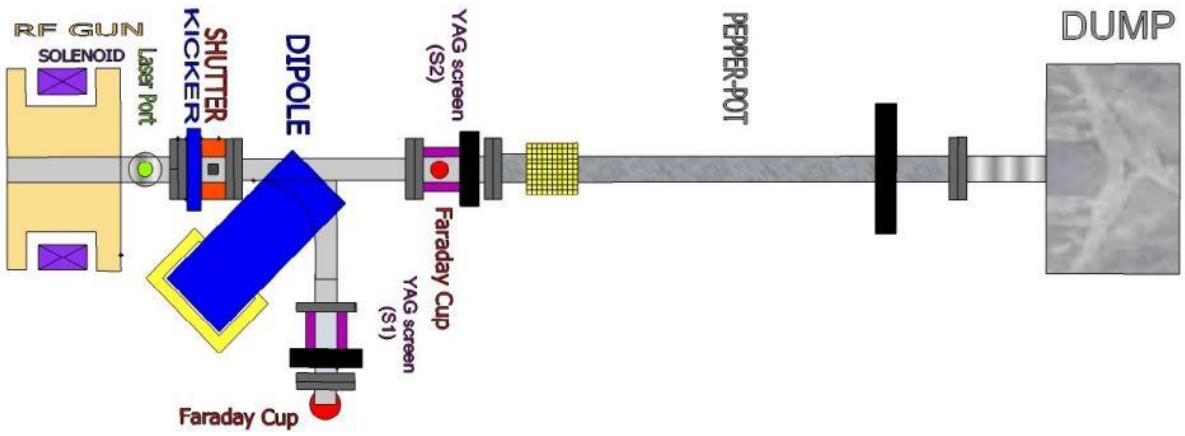

Figure 2.4: Layout of AREAL gun section with diagnostics (beam energy is 5 MeV)

$20\mu m$ thick YAG: Ce scintillation screens do not emit a significant amount of radiation to pose a problem from the radiation safety point of view. The radiation produced by “Pepper pot” is coating. Beam chamber walls at the bending magnet produce radiation only when the magnet is not operating in a stationary condition and beam hits or scraps vacuum chamber walls. The main sources of radiation are Faraday Cups at the ends of spectrometer arm and “Pepper pot”.

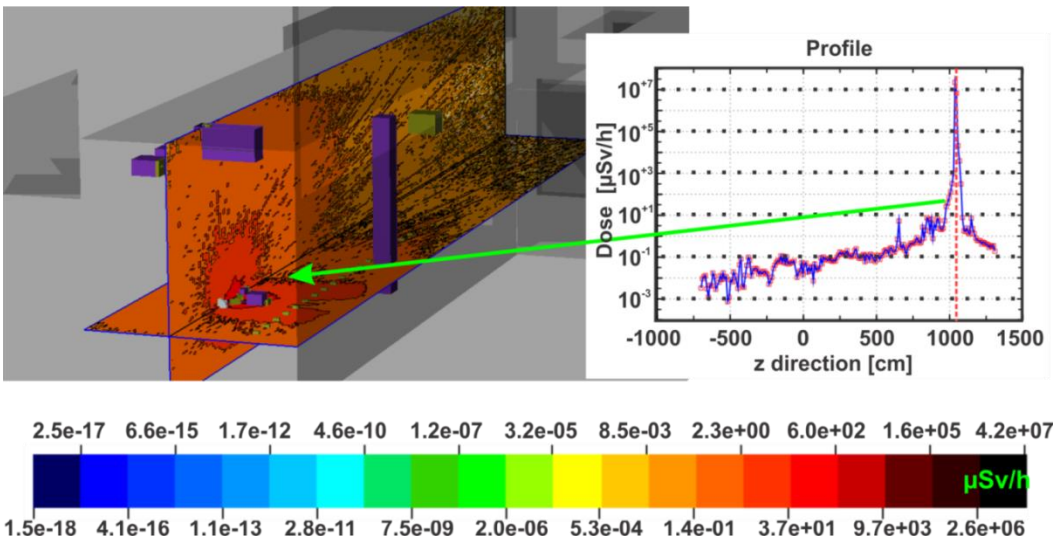

Figure 2.5: Equivalent dose distribution in the Tunnel in picSievets per electron hitting the Faraday Cup at the 95cm distance from the electron gun for 5 MeV beam energy (FLUKA simulation). Radiation penetrated tunnel walls carries $7.6 \cdot 10^{-5}\ MeV$ energy per electron.

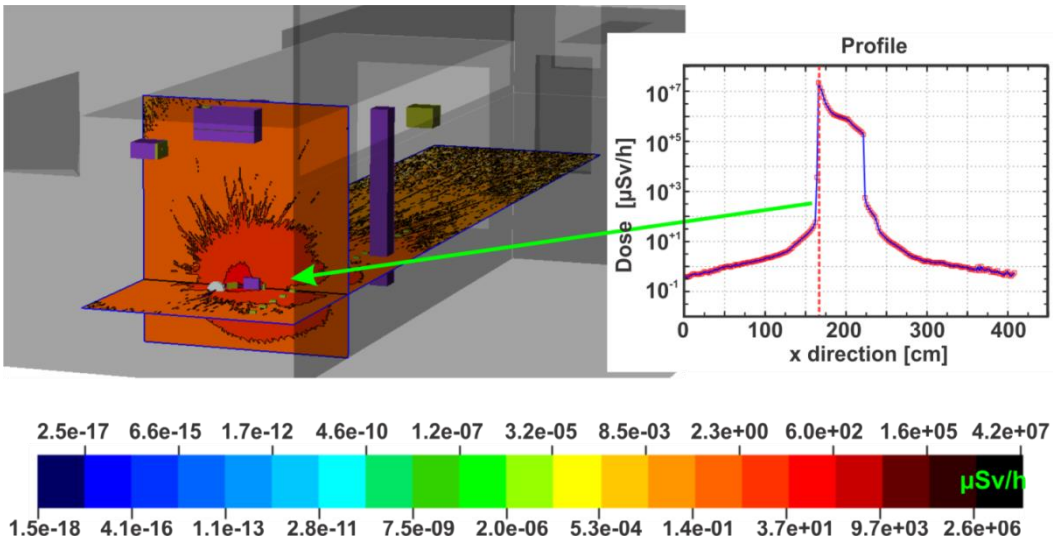

Figure 2.6: Equivalent dose distribution in the Tunnel in picSievets per electron hitting the Faraday Cup at the end of bend section for 5 MeV beam energy (FLUKA simulation). Radiation penetrated tunnel walls carries $5.5 \cdot 10^{-5}\ MeV$ energy per electron.

Faraday Cups consist of a hollow stainless steel cylinder of $15\ mm$ diameters, closed at the base, with an appropriately-sized aperture for collecting the electrons. An outer, grounded cylinder provides shielding.

Only 10^{-5} part of energy per electron incident on Faraday Cup escapes the tunnel as a gamma background radiation.

Ones we aim to get an ambient dose of $0.125\ microSieverts/hour$ outside machine tunnel, $100\ cm$ total thickness of concrete shielding will suffice ($50\ cm$ dump shielding plus $50\ cm$ wall). The insertion of $10\ cm$ Led shielding around dump reduces the concrete thickness to $50\ cm$. It includes also the contingency that takes into account possible deviations of the concrete parameters from the design values, e.g. density, homogeneity, isotropy, and chemical composition.

2.13 Numerical Simulation Study of the Radiation Field at AREAL

The determination of the radiation dose at linear accelerator AREAL ($\leq 5MeV$) facility and the comparison of the numerical simulation results with those of experimental measurements. The detailed characteristics of geometry have been taken into account. The computer program based on the FLUKA particle tracking simulation code was created and used to simulate radiation dose of the electron beam with $3.7MeV$ energy. The custom routines in FORTRAN language were programmed to define the 3D magnetic field in FLUKA, output beam parameters and input parameters of the primary electron beam respectively. Obtaining simulation results in a format suitable to compare with data measured in the experiment via Faraday Cup (which measures beam charge), YAG screen (which measures beam profile) and dosimeter (ion chamber) possible only using custom routines. The beam electrons interact with materials located on the trajectory (beam dump target, vacuum chamber walls, detectors, and diagnostic equipment), which leads to the generation of secondary radiation. Therefore, to determine the radiation dose field FLUKA particle transport code (based on Monte Carlo algorithm) has been used. A range of applications of FLUKA used in current study covers particle accelerator shielding, target design, dosimetry, detector design, etc. Since it is based on modern physical models, FLUKA can simulate the interaction and propagation in a matter of beam electron initiated electromagnetic shower comprising of photons and electrons down to 1 keV. FLUKA can handle complex geometries and track correctly

charged particles in the presence of magnetic or electric fields which is important in accelerator-related tasks, particularly that feature was used in the current study to transport the beam through the focusing solenoid and bending dipole magnets field. The SimpleGeo package is used to obtain a radiation profile on the electron beam line and 2D plot of dose distribution[94]. The entire assembly model of the AREAL premises and facilities is shown in **Figure 2.7(a,b)**, as it was developed with the help of SimpleGeo 4.3 software tool integrated with FLUKA that allows creating geometric models for FLUKA in a flexible and straightforward way.

The simulated electron beam had a Gaussian profile with Full width at Half Maximum (FWHM) $2.3 - 3.2mm$ in the x and y direction respectively and energy spread 1%. The numerical calculations are performed using the parameters of the electron beam given in **Table 2.3**.

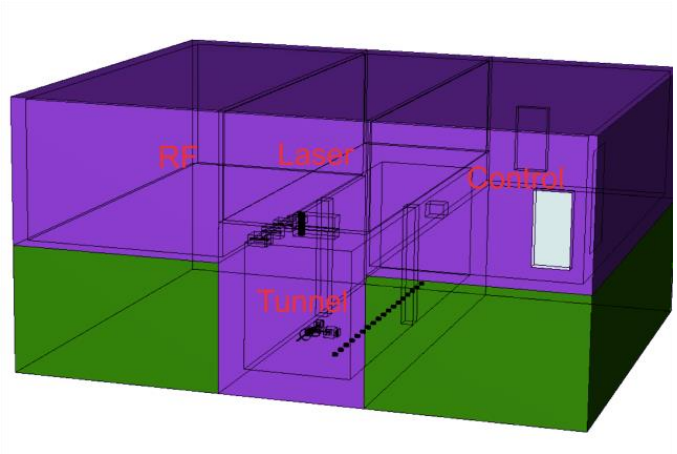

Figure 2.7a:The geometric model of the AREAL machine hall and neighboring rooms

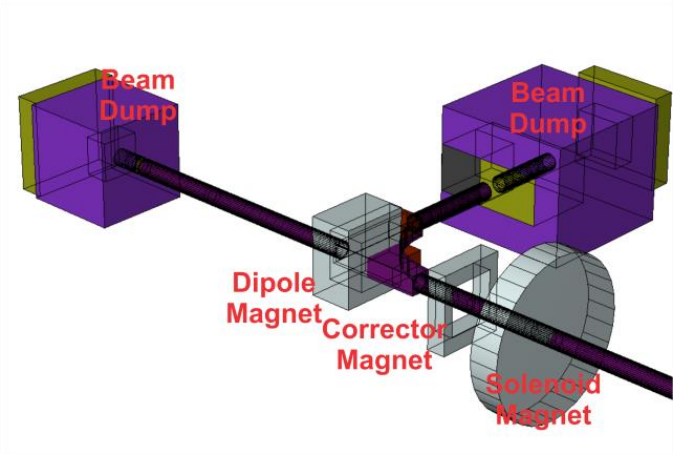

Figure2.7b: Accelerator facility equipment used in FLUKA simulations.

Table 2.3: Beam parameters

Energy	$E = 3.7\ MeV$
Direct bunch charge FC1	$250\ pC$
Bent bunch charge FC2	$36\ pC$
Bunch length	$0.4 - 9\ ps$
Norm. emittance	$\leq 0.5\ mm - mrad$
RMS energy spread	$\leq 1.5\%$
Repetition rate	$12\ Hz$

In this dissertation paper, experimentally measured data of dose rate by ion chamber and diagnostic equipment FC and YAG screens are compared with those of FLUKA simulations. FLUKA does not have built-in scoring cards letting the comparison of simulation with experiments. For that reason, custom routines were developed in order to modify FLUKA source code and obtain the data, which could be compared with experiments. Routines were used to simulate electron beam matching as close as possible to AREAL beam bunch and magnetic field of solenoid, corrector and dipole magnets. In addition, FLUKA output format has been changed to get the beam particles information such as coordinates, momentum and particle type at FC and YAG screen detectors region. Also, several FLUKA routines (magfld.f, mgdraw.f, source.f) were modified to match AREAL setup geometry. For the accurate modeling of the AREAL linear accelerator beam interaction with the environment, numerical simulation with FLUKA is performed applying the special settings by activating the following FLUKA command cards:

- DEFAULTS card - issued the PRECISIO scenario for the precision simulations;

- SOURCE card - to generate a distribution for source particles (beam profile, directional and energy distribution). This command activates calls to the user routine source.f
- EMF-CUT card - to establish secondary electron and photon transport. The cut off the energy of particle transport was set at 6 keV.
- USERDUMP card - the routine writes complete information of dump (the type of particles, trajectory, particles' energy). This command activates calls to the user routine mgdraw.f
- MAGFLD card - to use a magnetic field map.

The simulated electron beam had a Gaussian profile with Full Width at Half Maximum (FWHM) equal to $2.3 - 3.2\ mm$ in the x and y direction respectively and the energy spread 1%.

2.14 Experimental Setup

An ionization chamber survey meter dosimeter is being used routinely for the experimental measurement of dose rate in the machine tunnel. The instrument consists of air-opened $600\ cm^3$ large volume ionization chamber and low noise ampere meter circuit that provide high precision and a wide range of measurements of the ambient dose equivalent $H*(10)$, directional dose equivalent $H(0.07\Omega)$ and their rates. Since ionization chamber is integrating device it can cope with high-frequency gamma and beta radiation pulses produced by RF gun beam. Technical specification of dosimeter is given in **Table 2.4**.

Table 2.4: Technical specifications of the survey meter

Dose rate range Dose range	$0\ \mu Sv/h - \ 2000\ mSv/h$ $0 - 2000 \mu Sv$
Photon energy range Beta energy range	$6keV\ to\ 7.5\ MeV$

	$60keV\ to\ 2\ MeV$
Sensitive volume Lateral shielding Face entry window	$600\ cm^3$ disposable, $550\ mg/cm^2$ $3.3\ mg/cm^2$(metal covered PETP foil)
Accuracy Linearity	$< 15\%$ $\pm 5\%$

Dose rate in the tunnel is obtained by measurement using STEP OD-01 survey meter dosimeter at several different locations. **Figure 2.8** shows the schematic layout of the tunnel of the AREAL and the locations where the dose rate was measured. AREAL linac with beam diagnostic system consists of the laser-driven RF gun, focusing solenoid, bending magnet, corrector magnet, Faraday Cups (FC) and YAG screen. One of FC is located at the end of the curved pipe after the vacuum window and the second one (an insert able FC and YAG screen) is installed after the bending magnet in the straight section.

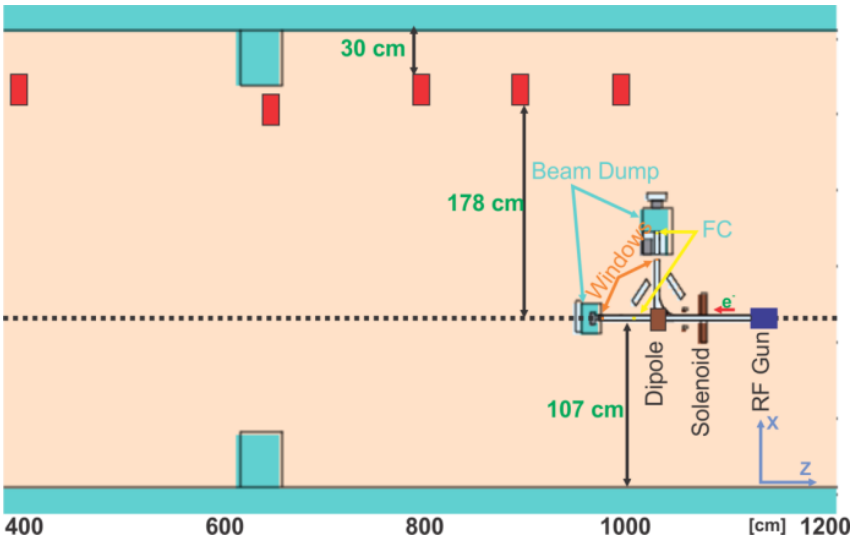

Figure 2.8: Layout of the AREAL linear in the horizontal (X,Z) plane Z axis points to the electron beam propagation primary direction. The red triangles show the positions of the dosimeter.

The beam energy measurement has been conducted using 90^0-degree bending magnet, which is located after the focusing solenoid. The energy spread is calculated using a bunch horizontal size on the YAG screen. **Table 2.3** gives the parameters of the electron beam obtained by beam diagnostic measurement when the dose rates in the tunnel have been measured.

It is found out that the dose rate varies in the tunnel depending on whether the bending magnet is switched on or off. Therefore, two series of the dose rate measurement results have been obtained corresponding to two cases when the bending magnet is switched on and when it is switched off. **Figure 2.9** shows the measurement results in both straight and bent beams cases. The position of the exit of RF gun coincides with $Z = 0$ coordinate. On each bar of the plot, the dosimeter position and dose rate values are indicated.

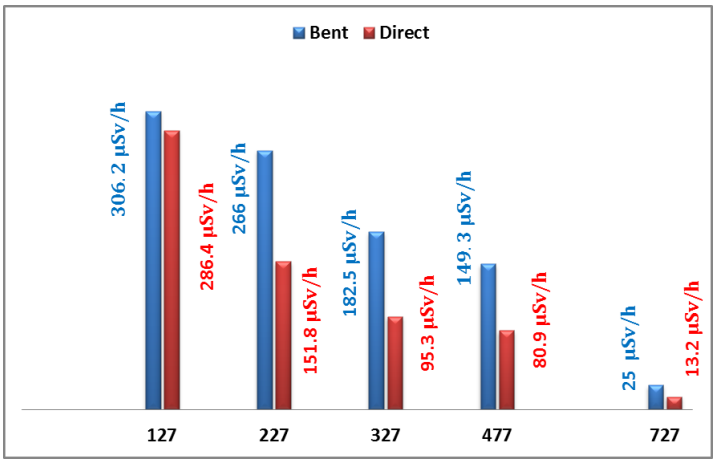

Figure 2.9: Measured dose for the various positions of the dosimeter corresponding to the straight beam (blue) and bent beam (red).

2.15 FLUKA Simulation Results Comparison with Experiment

Figure 2.10 shows the beam profile and the distribution of the energy distribution in three different positions. **Figure 2.10a, 2.10c** and **2.10e** demonstrate the electron beam transverse profile evolution along the curved beam line. **Figure 2.10a** shows the profile of the initial electron beam (x, y) at the end of the RF gun. **Figure 2.10c** depicts the 90-degree bent beam profile after bending magnet. Its horizontal width increased

due to dispersion. **Figure 2.10 e** demonstrates beam profile in the cross-sectional plane of the FC located on the bent beam section at a $20cm$ distance from the vacuum window inside the dump. Because of the interactions of the beam electrons in the $50\ \mu m$ tick Titanium window $20\ cm$ width air gap numerous halo electrons come to existence filling the beam pipe inner volume.

Figure 2.10b, 2.10d and **2.10f** demonstrate energy distribution of the electron beam at (mentioned above) three different positions. The histograms are normalized to the maximum of the first histogram (referring the primary beam). The bent beam (**Figure 2.10d**) contains only 74% of the initial number of the particles. Comparing **Figure 2.11b** with **Figure 2.10d,** one can conclude that 90^0-degree bending preserves the beam initial energy spread (FWHM is $\sim 2.7\%$). It can be seen that only 21% of initial particles survive the interaction processes when the beam propagates through the Titanium window and $20cm$ air layer.

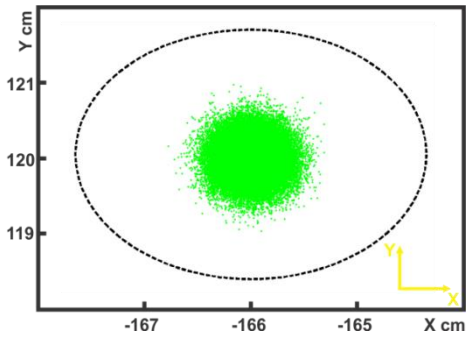

Fig. 2.10 a) The profile of the initial electron beam (x, y) at the end of the RF gun

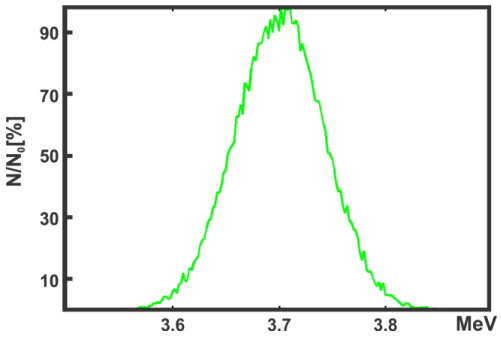

Fig. 2.10 b) The energy distribution of the electron beam at the end of the gun.

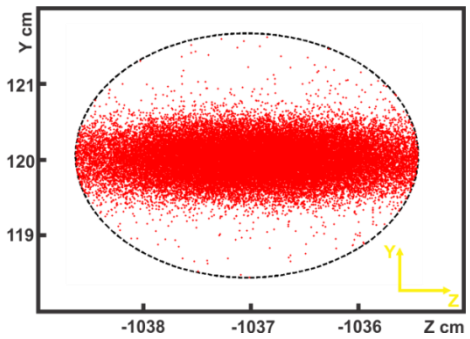

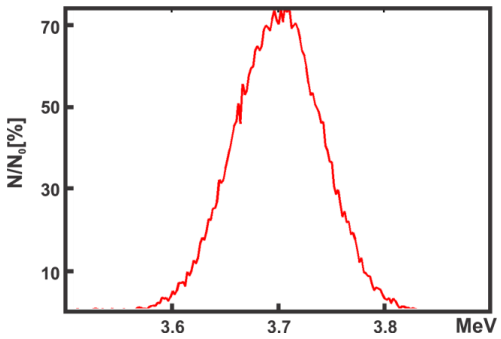

Fig. 2.10 c) The beam profile in the plane of the YAG screen target located between bending magnet and the vacuum window.

Fig. 2.10 d) The energy distribution of the electron beam at the YAG screen target located between the bending magnet and the vacuum window.

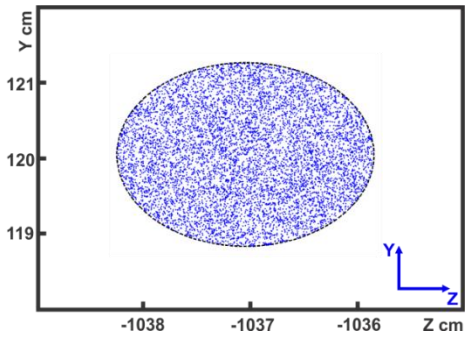

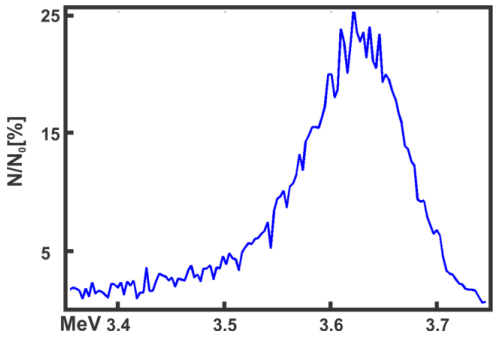

Fig. 2.10 e) The beam profile in the cross-sectional plane of the FC located on the bent beam section at a 20cm distance from vacuum window inside the dump**.**

Fig. 2.10 f) The energy distribution of the electron beam at the FC located on the bent beam section at a 20cm distance from vacuum window inside the dump.

Figure 2.11 and **Figure 2.12** illustrate that taking 1% RMS for beam energy spread in numerical simulations yields dose rates values closer to those of obtained by measurements. One of the reasons of some mismatch between measured and simulation results is the fact that it is virtually impossible to take into account the precision of some elements of geometry such as PC or cables and other infrastructure equipment in digital models.

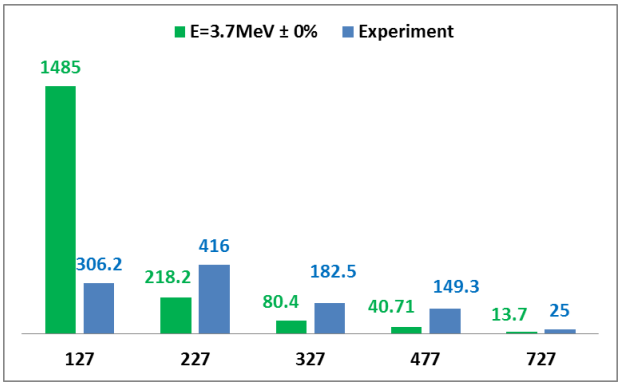

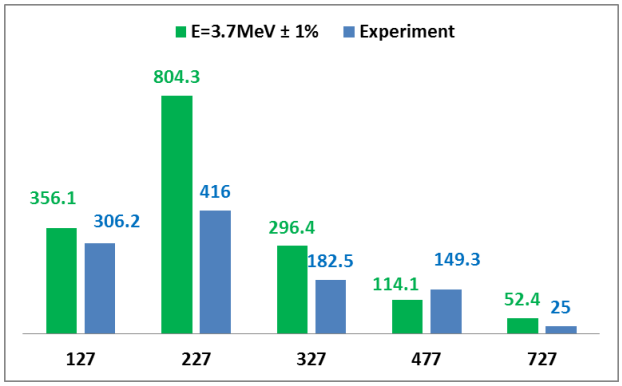

Figure 2.11: Calculated and measured dose rates in μSv/hr for some position of the dosimeter for the bent beam, when primary energy spread was 0%(left) and when

energy spread was 1% RMS (right). The horizontal axis is the distance from the gun exit in cm.

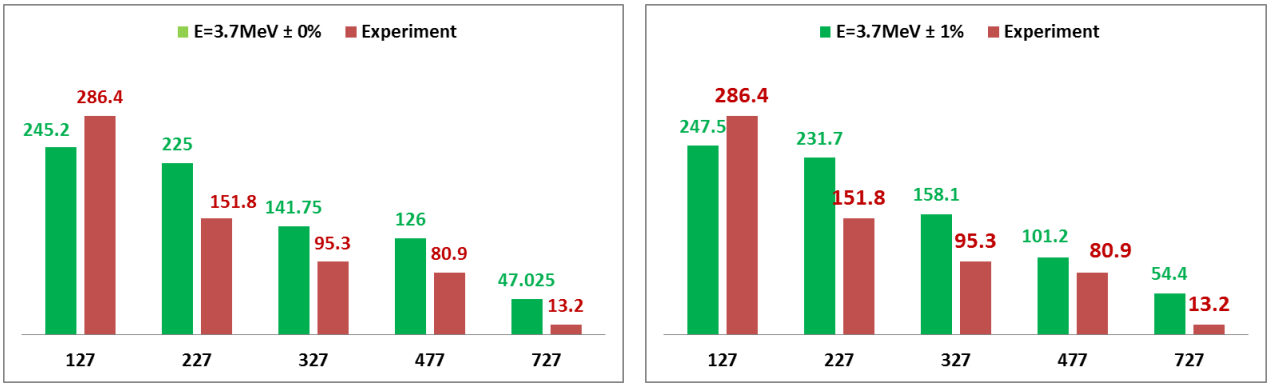

Figure 2.12: Calculated and measured dose rates in μSv/hr for some position of the dosimeter for straight beam, when primary energy spread was 0%(left) and when the energy spread was 1% RMS (right). The horizontal axis is the distance from the gun exit in cm.

2.16 Conclusions

FLUKA simulations of the secondary radiation field at AREAL machine hall and experimental rooms were performed. Input parameters for the simulation beam derived from the beam diagnostic measurements (e.g. beam current is given by FC measurement). Radiation measurement was performed using ion chamber that can measure gamma, electron and positron fluxes produced by the pulsed source. Dose rate measurement results have been compared with the values of numerical simulations and satisfactory agreement has been found, thus validating the choice of the simulation method. Dose measurement data was used to improve the accuracy of the beam diagnostic data. Particularly, it was found that the beam initial energy spread was about 1.5%. Dose rates continuous measurement with ion chamber helps monitor and control the radiation level. Radiation safety considerations imply monitoring and management of the radiation level within the machine hall and neighbouring rooms. At the current stage of the AREAL development, the beam energy is in the range of $5\ MeV$, well below the threshold of the neutron, production channel via giant dipole mechanism. Therefore,

eventually, only gamma component of the penetrating radiation exists, taking into account electrons and positrons short paths at those energies. Numerical simulation and dose measurement gave data allowing the development of the necessary radiation shielding and protection walls and proved that radiation dose levels in the AREAL machine hall and experimental rooms conform the radiation safety requirements for equipment and personnel.

SUMMARY

- FLUKA simulations of the secondary radiation field at AREAL machine hall and experimental rooms have been performed. Input parameters for the simulated beam have been derived from the beam diagnostic measurements.
- Dose rate measurement results have been compared with the values of numerical simulations and satisfactory agreement has been found thus validating the choice of simulation method.
- Dose measurement data were used to improve the accuracy of the beam diagnostic data. It was found particularly that the beam initial energy spread was about 1.5%.
- Numerical simulation and dose measurement gave data allowing development of the necessary radiation shielding and protection walls to ensure that radiation dose levels in the AREAL machine hall and experimental rooms conform to the radiation safety requirements for equipment and personnel.

Chapter 3: The Radiation Exposure Time and Absorbed Dose Distribution for the Irradiation Experiments at the AREAL Electron Linac

3.1 Introduction

The paper concerns the study of the ~5 MeV electron beam interaction with the thin layer experimental sample at the AREAL electron linear accelerator. The necessary exposure time and the irradiation effects parameters calculations have been performed using measured parameters of the beam and numerical simulations applying particle transport code FLUKA [11]. Numerical simulations with FLUKA provide the estimation of the absorbed dose - the main parameter that defines the amount of the radiation-induced crystalline structure defects. Calculations have been conducted for the experimental study of the irradiation effects on the parameters of the ferromagnetic composition $Ba_{75}Sr_{25}TiO_3$ - Barium-Strontium-Titanate (BST) thin film[95-99]. The main goal reached is the calculation of the required exposure time taking into account the beam intensity, energy, spatial and angular distributions, and experimental sample geometrical shape, size, composition, and disposition for obtaining the intended value of the absorbed dose. Beam parameters used for numerical simulations have been obtained from beam diagnostic measurements.

Ferroelectric thin films, particularly BS-based ones, have wide applications in multifunctional microelectronic devices [22-23]. The electric, dielectric, and Ferro-electric characteristics of these thin films can be modified via electron irradiation leading to microelectronic devices new performance [24–28]. The BST thin films have a low-frequency dependence of the relative permittivity and dielectric losses. Those dependencies can be substantially changed by the samples electron irradiation producing thin films with the properties adapted to the requirements of the application. The 4 MeV electron beam irradiation effects on the electric, dielectric, and ferroelectric

properties of the BST film-based sensor (**Figure3.1**) have been studied in the frequency range from 100 Hz to 1 MHz.

An experimental study has been carried out at the AREAL linear accelerator aiming at the investigation of the effect of the irradiation by the 4.2 MeV electron beam on the electrical properties of the ferroelectric composition $Ba_{75}Sr_{25}TiO_3$ (BST). The paper is focused on the methods of the calculation of experimental sample irradiation parameters based on the beam parameters measurement and numerical simulation study of the electron beam interaction with the BST material thin layer (**Table 3.1**).

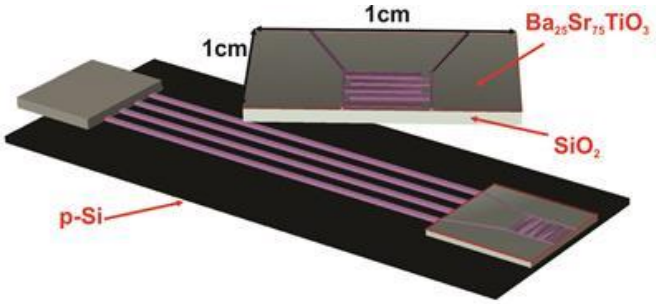

Figure 3.1: Structure and parameters of the experimental sample

Material	Thickness
$Ba_{75}Sr_{25}TiO_3$	300 µm
SiO_2	500 µm
p-Si	0.6 mm

Table 3.1: Structure of the experimental sample

The experimental sample consists of three thin layers of a rectangular cross-section with different sizes and chemical composition (BST, SiO_2 and p-conductivity Silicon). **Figure 3.1** shows the parameters and the layer structure of materials.

AREAL electron linac can produce clean and controllable 2-5 MeV electron beam with 10- 250 pC bunch charge and 1- 50 Hz repetition rate [71].

The duty factor D_f is the fraction of operating time during which the accelerator is actually producing radiation, which can reach to 5×10^{-11} for the AREAL linac first stage installation. It is the product of pulse repetition rate p (in Hz) and pulse length T_p (in seconds):

$$D_f = T_p \times p.$$

The main parameters of the electron beam can be monitored and manipulated to apply precise irradiation dose for the experimental sample. Main parameters of the AREAL electron beam are presented in **Table 3.2**.

Table 3.2: AREAL beam parameters

Energy	2–5 MeV
Bunch charge	10–250 pC
Bunch length	0.4–9 ps
Norm. emittance	≤ 0.5 mm-mrad
RMS energy spread	≤1.5 %
Repetition rate	1–50 Hz

3.2 Beam Diagnostic Measurements

Advanced Research Electron Accelerator Laboratory (AREAL) based on photocathode RF gun is being constructed at CANDLE.

The AREAL RF photo gun experimental operation provides the electron bunches with 4.2 MeV energy and 250 pC beam charge. The gun section contains the focusing solenoid, magnetic spectrometer, horizontal/vertical corrector magnet, Faraday Cups (FC) and YAG screens with cameras. The charge of individual bunches was measured using two FCs.

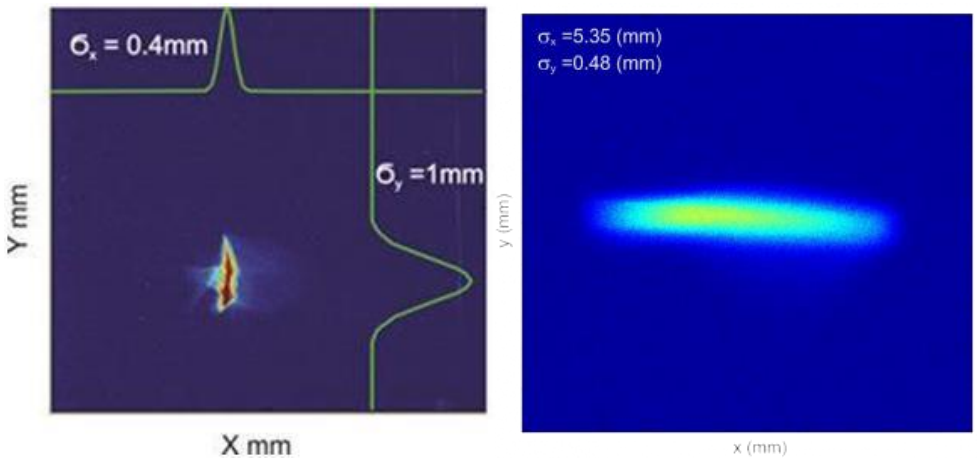

Figure 3.2: Electron beam profiles downstream to photo-injector measured by YAG screen system at straight section(left) and at spectrometer section (right).

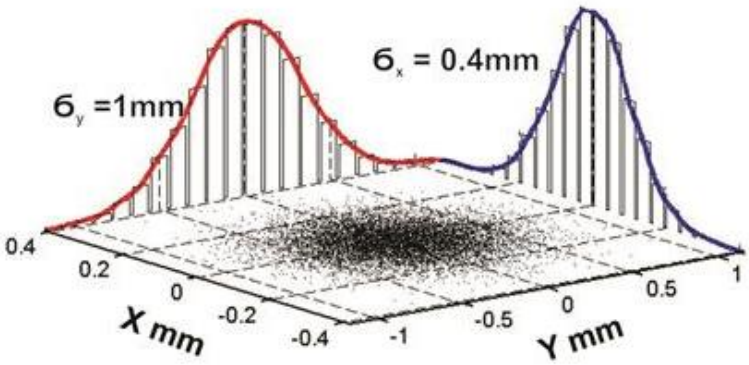

Figure 3.3: The profile of the electron beam along the horizontal and vertical axes perpendicular to the beam direction at the beam pipe window.

The beam energy and the energy spread measurements have been performed using the magnetic spectrometer located after the gun focusing solenoid. The spectrometer consists of 90° bending dipole magnet and the YAG screen. The beam absolute energy is determined by measuring the bunch position with respect to the central trajectory, which was calibrated with particle tracking simulations using the measured dipole magnetic field distribution. The energy spread is evaluated using the bunch horizontal profile at the YAG screen.

Figure 3.2 presents the 250 pC charge beam profile at the YAG screens located downstream to the injector. The corresponding beam energy is about 4.2 MeV and the

energy spread is below 2%. Beam transverse profile measurements results have been used (**Figure 3.3**) to calculate absorbed dose spatial distribution. The particles energy spread is dominated by an uncorrelated contribution, which is decreasing during acceleration inversely proportional to beam energy.

The barium strontium titanate ceramics has been irradiated by 4.2 MeV electron beam at the AREAL. The samples were exposed to the electron beam at a distance of 3cm from the exit port.

3.3 Numerical Simulation with FLUKA

Absorption dose in the sample through the electron has been calculated using the particle transport simulation code FLUKA. The results of beam diagnostic measurements used for simulations include:

a) Beam current measurements by Faraday cup

b) Beam transverse profile monitoring by YAG screen and camera station

c) Focusing solenoid magnet current adjustment and definition of the beam minimal spot size

d) Beam energy/momentum measurement by spectrometer consisting of dipole magnet and YAG screen system.

Figure 3.2 shows that the beam has a Gaussian distribution of electrons along horizontal and vertical directions, i.e. perpendicular to the beam direction. Default function of FLUKA does not let to simulate the beam with required parameters. The default function is designed to calculate physical quantity per electron that gives only integral values of absorbed dose. Therefore, a custom user routine was programmed in FORTRAN language. The program is able to generate the beam with the parameters and distributions that is actually available at AREAL linear accelerator. **Figure 3.5** shows the profile of the electron beam, used for the FLUKA simulations.

It was obtained from the FLUKA numerical simulations that the number of electrons incident on the experimental sample is 58.65 percent of the electrons beam

that has reached the beam pipe exit port. Missing electrons have been absorbed by the 50 microns tick titanium exit window while traveling the distance of 3 cm in the air. Only 12.66 percent of the electrons that reached the BST layer have been scattered within the layer volume. Most of the electrons passed through the material without any interaction. **Figure 3.4** shows the electron energy distribution changein the result of the interactions of the electron beam with the BST layer. Distribution curve shift towards lower energies corresponds to the energy loss within the BST layer.

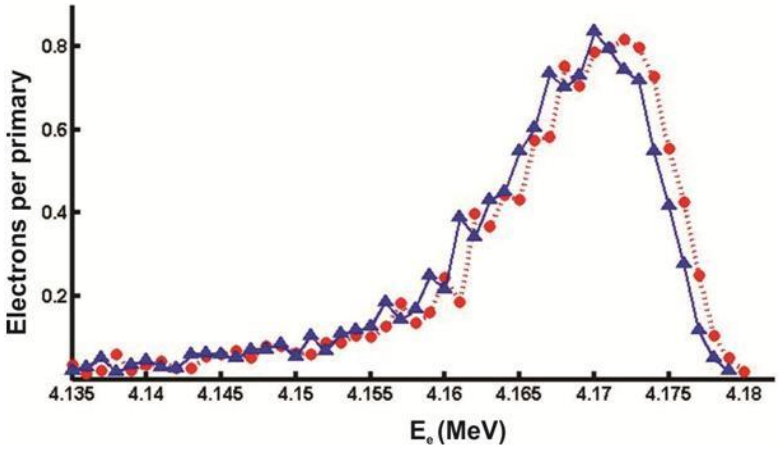

Figure 3.4: Electron beam energy spectrum before (circles) and after (triangles) interaction with the BST layer obtained by numerical simulation. Distributions are normalized per primary.

It can be seen that the energy losses of those electrons that interact with the matter are insignificant compared to their initial energy. **Figure 3.5a** presents the absorbed dose (per electron) distribution along beam direction within the BST layer. The total absorbed dose in $Ba_{75}Sr_{25}TiO_3$ is 3.48 $\times 10^{-8}$Gy per electron per second. In **Figure 3.5b** dose distribution in whole experimental sample setup including all layers is depicted whereas in **Figure 3.5a** dose distribution only in $Ba_{75}Sr_{25}TiO_3$.

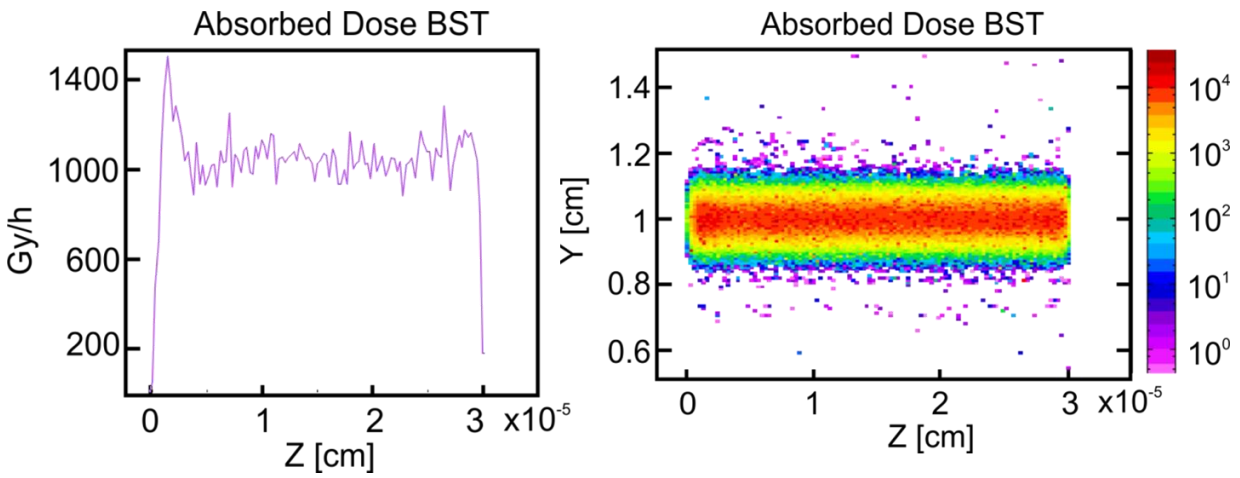

Figure 3.5a: Absorbed dose (unit: Gray = 1 J/kg) calculated distribution within the BST layer. The Z points to the beam direction.

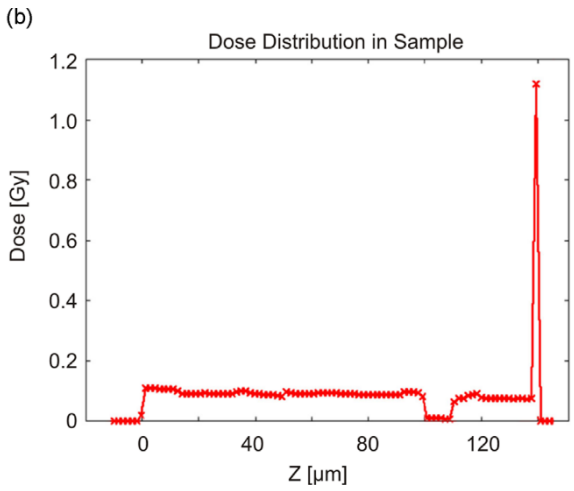

Figure 3.5b: Dose distribution in all three layers of experimental setup per primary particle. Spike corresponds to $Ba_{75}Sr_{25}TiO_3$.

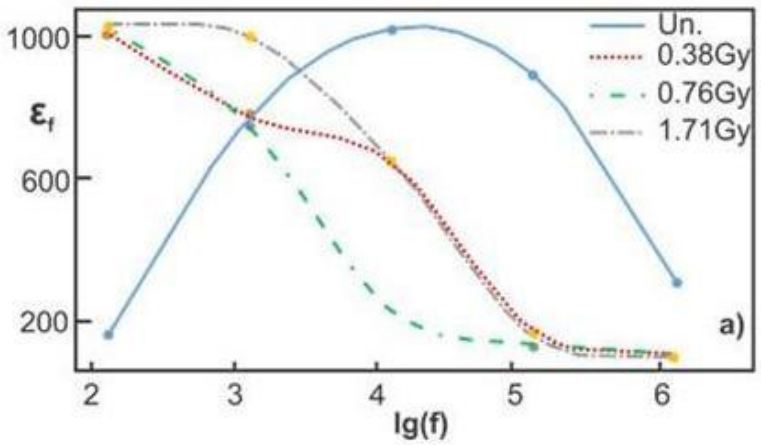

Figure 3.6: Measured dependence of dielectric permittivity on frequency for unirradiated and electron-irradiated $Ba_{75}Sr_{25}TiO_3$ thin films.

3.4 Dielectric Properties of BST Thin Films

The variation of room temperature dielectric permittivity with frequency for unirradiated and electron irradiated (for delivered dose of 0.38, 0.76 and 1.71 Gy) $Ba_{75}Sr_{25}TiO_3$ thin films are as shown in **Figure 3.6**. There is a remarkable change in the dielectric permittivity behavior after irradiation with various delivered doses. The room temperature dielectric permittivity of unirradiated BST thin films at 2kHz is 100. It has been observed to increase with the increase of delivered dose. The dielectric loss showed significant frequency dispersion for both unirradiated and electron irradiated films. Experimental measurements have been conducted using high resistance meter with the threshold of $10^{-6}\Omega$ and LCR meter with the frequency range up to1 MHz.

3.5 Bio-medical Applications

Innovative experimental in vitro investigations in radiobiology are of crucial importance for understanding the basic mechanisms of radiation damage of the cell. The 2–5 MeV energy AREAL ultra-short electron bunches are a very appropriate tool for precise and controllable studies in radiation biology and medical physics in a wide range of applied radiation doses [100-104].

AREAL machine set-up provides a good basis for the facility development and the start-up of the first experiments. The facility has two in-air experimental stations H1 and

H2 for applied research in the fields of life and materials sciences. The first station H1 with a focused electron beam is located downstream of the linac. The second station H2 is designated for the electron energy correlated experiments and is located after the magnetic spectrometer in order to avoid the dark current effects.

An important issue of the electron irradiation experiments is the spatial and absorbed (by sample) dose distributions. The experimental studies at AREAL have been supported by modeling the dose distributions using the FLUKA [32] code. The numerical simulations have been compared to the measurements. Fig. 3.7 shows the radiation field spatial distribution (experimental station H1) for the incident electron beam energy of 3.6 MeV and 250 pC charge. As is seen, the radiation is concentrated in the sample region. The simulated absorbed dose distribution at the experimental station H1 within the biological sample (water equivalent) along the horizontal and perpendicular axis of beam direction is given in Fig. 3.8. The calculated total absorbed dose for water-filled cylinder of 1 cm diameter and 2 cm length is 0.37 Gy, while the measured ambient dose equivalent in the vicinity of the biological sample is 0.34 Gy. The simulated and measured absorbed doses coincide within 10%.

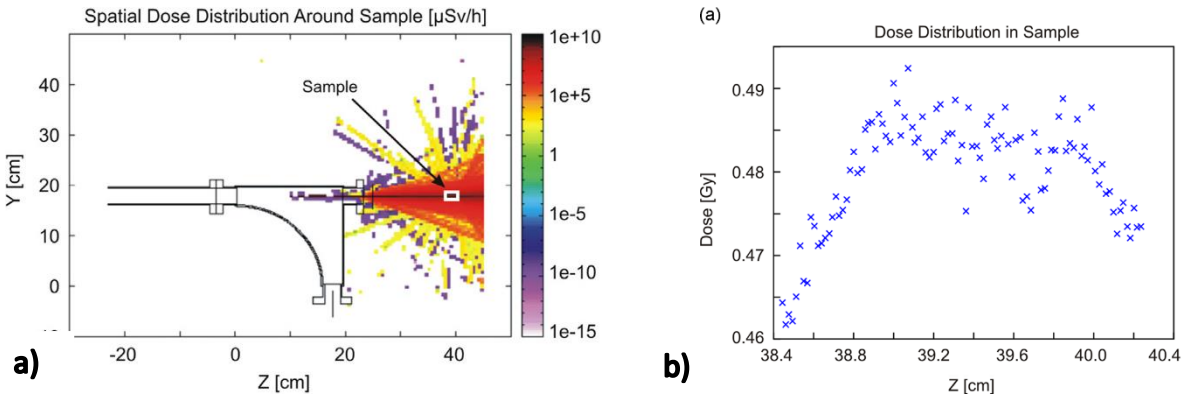

Figure 3.7 a: Radiation field spatial distribution at experimental station H1 (a) and (b) absorbed dose (unit: Gy/h) distribution within the biological sample along the horizontal axis pointing to beam direction

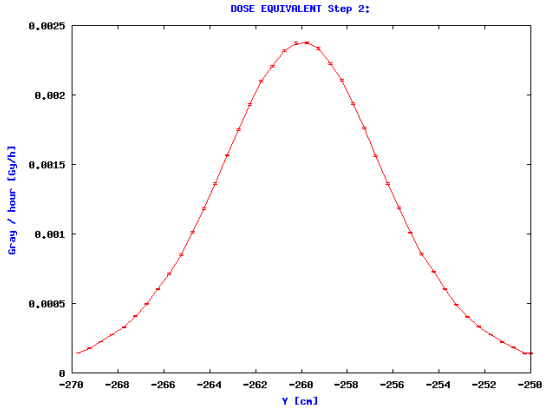

Figure 3.8: Absorbed dose (unit: Gy/h) distribution within the biological sample along the perpendicular.

3.5 Summary

- FLUKA simulations has been conducted aimed at calculation of the required exposure time to provide necessary irradiation dose for the given beam parameters (energy, current, spatial sizes and divergence).
- Beam diagnostic measurements results have been combined with the experimental sample geometrical and composition parameters and digital simulations of the electronic beam interaction with the experimental equipment have been performed.
- Absorbed dose spatial distributions within the volume of the experimental samples have been found via digital simulations. Calculated absorbed dose spatial distribution within the volume of the BST thin film has turned to be essentially uniform.

Acknowledgments

I do express my deepest and sincere gratitude to my supervisor Vitali Khachatryan for guidance during my research and giving me opportunities to do my research. His contribution was invaluable in my professional growth. His visions motivated me during my research work and played important role. He taught me methodology on how to do a research and present it in the most accessible way to public. My research couldn't not be finished without his support.

Acknowledgments

I would like to express my gratitude to everyone who has supported me during the course of this thesis.

I want to express my thanks to Prof. V. Tsakanov, without whom this dissertation could not be accomplished.

I would also like to express my gratitude to Z. Amirkhanyan, who has helped me during all the work period.

I am also grateful to the stuff of CANDLE SRI for their constant support and assistance.

References

1. M. Altarelli et al., XFEL: The European X-Ray Free- Electron Laser, Technical Design Report, DESY 2006-097, Hamburg, 2006.
2. S. Schreiber, et al., FEL user facility FLASH, in: Proceedings of the IPAC'10, Kyoto, Japan, pp. 2149–2152.
3. Linac Coherent Light Source (LCLS) Conceptual Design Report, SLAC–R–593, p. 554 (2002).
4. T. Bizen, T. Tanaka, Y. Asano, D. E. Kim, J. S. Bak, H. S. Lee and H. Kitamura, "Demagnetization of undulator magnets irradiated high energy electrons," Nucl. Instrum.Meth.A 467(2001) 185.
5. K. Nakamura,K. Hagiwara,K. Hikasa,H. Murayama,M. Tanabash et al., JPG 37, 075021 (2010) (http://pdg.lbl.gov]
6. V.I.Telnov, "Scattering of Electrons on Thermal Radiation Photons in Electron - Positron Storage Rings". Nucl.Instrum.Meth. A260 (1987) pp.304-308.
7. M. Minty, F. Zimmermann, Beam Techniques-Beam Control and manipulation, SLAC – R-621, (2003).
8. H. Schlarb, "Design and performance of the TESLA Test Facility collimation system," AIP Conf. Proc. 693 (2004) 209, EPAC'02, Paris, June 2002.
9. T. Kamps, "Collimation System for the BESSY FEL", Proceedings of the FEL Conference, 2004 Trieste, Italy, 381-384.
10. V. Khachatryan, **V. Petrosyan**, T. Vardanyan, "Particle Tracking Simulations for EXFEL Complex shape Collimators" Proceedings of FEL14, Basel, Switzerland 2014, p.22-25 (2015).
11. A. Ferrari, P.R. Sala, A. Fassò, J. Ranft, "FLUKA: a multi-particle transport code", CERN 2005-10 (2005), INFN/TC_05/11, SLAC-R-773.
12. V. Khachatryan, **V. Petrosyan**, A. Sargsyan, A. Tsakanian, "Particle Tracking Simulations with FLUKA for DESY FLASH and EXFEL Collimators" Proc. of IPAC2014, Dresden, Germany p. 363-365.

13. V. M. Tsakanov, G. A. Amatuni, Z. G. Amirkhanyan, et al., “AREAL Test Facility for Advanced Accelerator and Radiation Source Concepts“, Nuclear Instruments and Methods in Physics Research A, 284-290, 2016.
14. V.G. Khachatryan, **V.H.Petrosyan**, A.A.Sargsyan,” Radiation safety considerations for areal electron Linac with beam diagnostic system” Proceedings of IPAC2014, Dresden, Germany p. 1647-1649.
15. **V.H. Petrosyan**, “Interaction of the 5 MeV electron beam with the matter in the AREAL photoelectron gun facility experimental hall”, Armenian Journal of Physics, 2017, vol. 10, issue 4, pp. 163-170.
16. V. M. Tsakanov, R. M. Aroutiounian, G. A. Amatuni, **V.H.Petrosyan** et al., “AREAL Low Energy Electron Beam Applications in Life and Materials Sciences“, Nuclear Instruments and Methods in Physics Research A, v.829, pp. 248-253, 2016.
17. **V.H. Petrosyan**,” Absorbed Dose Characteristics for the BST Thin Film Irradiation by the 5 MeV Electron Beam”, Armenian Journal of Physics, 2016, vol. 9, issue 3, pp. 235-238.
18. FEL Beam Dynamics Group Home Page: http://www.desy.de/fel-beam
19. B. Grigoryan, G. Amatuni, V. Avagyan, A. Grigoryan, M. Ivanyan, V. Khachatryan, E. Laziev, K. Manukyan, I. Margaryan, T. Mkrtchyan, V. Sahakyan, A. Sargsyan, A. Tarloyan, A. Tsakanian, V. Tsakanov, A. Vardanyan, T. Vardanyan, V. Vardanyan, “Advanced research electron accelerator laboratory based on photocatode RF Gun”, Proceedings of IPAC2011, San Sebastian, Spain , pp 1066-1068 .
20. A. Fasso, A. Ferrari, J. Ranft, P.R. Sala FLUKA: present status and future developments Proc. IV Int. Conf. on Calorimetry in High Energy Physics, La Biodola (Italy) 21-26 September 1993, Ed. A. Menzione and A. Scribano, World Scientific, p. 493-502.
21. A. Fasso,A. Ferrari, P.R. Sala "Desiging electron accelerator shielding with FLUKA", 8th Int. Conf. on Radiation Shielding, Arlington (Texas) Apr. 24-28 1994, p. 643-649

22. A.K. Tagantsev, V.O. Sherman, K.F. Astafiev, J. Venkatesh, N. Setter,"Ferroelectric Materials for Microwave Tunable Applications", Journal of Electroceramics volume 11, pp 5-7 (2003)
23. S.Sh. Gevorgian, in Ferroelectrics in Microwave Devices, Circuits and Systems, Springer-Verlag, London, 2009.
24. S. Aparna, V. M. Jali, G. Sanjeev, J. Parui, S. B. Krupanidhi, "Dielectric properties of electron irradiated $PbZrO_3$ thin films",Bullet in Materials Science Volume 33 (3) (2010) pp. 191-196
25. V. A. Balakin, A.I.Dedik, S.F.Karmanenko et al. “The influence if electron beam on dielectric properties of ferroelectric BSTO films”, Pisma JTF, v.29, 2003, pp.77-83.
26. C.M. Othon, S.Ducharme,"Electron Irradiation Effects on Ferroelectric Copolymer Langmuir-Blodgett Films", Ferroelectrics volume 304 (2004) pp 9-12.
27. C.M. Othon, F.B.Bateman, S.Ducharme, "Effects of electron irradiation on the ferroelectric properties of Langmuir-Blodgett copolymer films",Journal of Applied Physics, volume 98 014106(2005).
28. I.Baturin, N.Menou, V.Shur, C. Muller, D.Kuznetsov, J.L.Hodeau, A.Sternberg, "Influence of irradiation on the switching behavior in PZT thin films" Materials Science and Engineering B Volume 120, (2005), pp. 141-145
29. G. Musiol, J. Ranft, R. Reif & D. Seeliger, Kern- und Elementarteilchenphysik, VCH Verlagsgesellschaft, Weinheim (1988)
30. W. Heitler, The Quantum Theory of Radiation, Clarendon Press, Oxford (1954).
31. B. Rossi, High Energy Particles, Prentice-Hall, Englewood Cliffs (1952)
32. B. Sitar, G.I. Merson, V.A. Chechin & Yu.A. Budagov, Ionization Measurements in High Energy Physics (in Russian), Energoatomizdat, Moskau (1988)
33. B. Sitar, G.I. Merson, V.A. Chechin & Yu.A. Budagov, Ionization Measurements in High Energy Physics, Springer Tracts in Modern Physics, Vol. 124, Springer, Berlin/Heidelberg (1993).
34. E.A. Uehling, Ann. Rev. Nucl. Sci. 4, 315 (1954) (For heavy particles with unit charge, but $e^{\pm}$ cross sections and stopping powers are also given).

35. "Stopping Powers for Electrons and Positrons," ICRU Report No. 37 (1984).
36. E. Segre, Nuclei and Particles, New York, Benjamin (1964) p. 65 ff.
37. Y.S. Tsai, Rev. Mod. Phys. 46, 815 (1974).
38. H. Davies, H.A. Bethe, and L.C. Maximon, Phys. Rev. 93, 788 (1954).
39. J.D. Jackson, Classical Electrodynamics, 3rd edition, (John Wiley and Sons, New York, 1998).
40. L.D. Landau and I.J. Pomeranchuk, Dokl. Akad. Nauk. SSSR 92, 535 (1953); 92, 735 (1953). These papers are available in English in L. Landau, The Collected Papers of L.D. Landau, Pergamon Press, 1965; A.B. Migdal, Phys. Rev. 103, 1811 (1956).
41. S. Klein, Rev. Mod. Phys. 71, 1501 (1999).
42. M.L. Ter-Mikaelian, SSSR 94, 1033 (1954); M.L. Ter-Mikaelian, High Energy Electromagnetic Processes in Condensed Media (John Wiley and Sons, New York, 1972).
43. P. Anthony et al., Phys. Rev. Lett. 76, 3550 (1996)
44. W.R. Nelson, H. Hirayama, and D.W.O. Rogers, "The EGS4 Code System," SLAC-265, Stanford Linear Accelerator Center (Dec. 1985).
45. B. Rossi, High Energy Particles, Prentice-Hall, Inc., Englewood Cliffs, NJ, 1952.
46. Experimental Techniques in High Energy Physics, ed. T. Ferbel (Addison-Wesley, Menlo Park CA 1987).
47. U. Amaldi, Phys. Scripta 23, 409 (1981).
48. E. Longo and I. Sestili, Nucl. Instrum. Methods 128, 283 (1975).
49. G. Grindhammer et al., in Proceedings of the Workshop on Calorimetry for the Supercollider, Tuscaloosa, AL, March 13–17, 1989, edited by R. Donaldson and M.G.D. Gilchriese (World Scientific, Teaneck, NJ, 1989), p. 151.
50. W.R. Nelson et al., Phys. Rev. 149, 201 (1966).
51. G. Bathow et al., Nucl. Phys. B20, 592 (1970).
52. T.T.Böhlen. F.Cerutti, M.P.W.Chin, A.Fassò, A.Ferraria, P.G.Ortega, A.Mairani, P.R.Sala, G.Smirnov, V.Vlachoudis "The FLUKA Code: Developments and Challenges

for High Energy and Medical Applications" Nuclear Data Sheets, volume 120, June 2014, Pages 211-214

53. T. T. Böhlen, F. Cerutti, M. P. W. Chin, A. Fassò, A. Ferrari, P. G. Ortega, A. Mairani, P. R. Sala, G. Smirnov, and V. Vlachoudis, The FLUKA code: Developments and challenges for high energy and medical applications, Nucl. Data Sheets 120, 211 (2014).
54. A. Fasso, A. Ferrari, S. Roesler, P.R. Sala, F. Ballarini, A. Ottolenghi, G. Battistoni, F. Cerutti, E. Gadioli, M.V. Garzelli, A. Empl, J. Ranft " The physics models of FLUKA: status and recent development", CHEP03, March 24-28, 2003, La Jolla, California,C0303241:MOMT005 2003
55. G. Battistoni et al., The FLUKA code: Description and benchmarking, in Proceedings of the Hadronic Shower Simulation Workshop 2006, Batavia U.S.A. (2006), AIP Conf. Proc. 896 (2007)
56. A. Fasso, A. Ferrari, J. Ranft and P.R. Sala ,"FLUKA: performances and applications in the intermediate energy range" Proc. of an AEN/NEA Specialists' Meeting on Shielding Aspects of Accelerators, Targets and Irradiation Facilities, Arlington (Texas) 28-29 April 1994. OECD Documents, Paris 1995, p. 287-304
57. K. Parodi et al., Patient study of in vivo verification of beam delivery and range, using positron emission tomography and computed tomography imaging after proton therapy, Int. J. Radiat.Oncol.68 (2007) 920.
58. G. Battistoni, V. Boccone, F. Broggi, M. Brugger, M. Campanella, M. Carboni, F. Cerutti, A. Empl, A. Fasso, A. Ferrari, A. Ferrari, et al.,"Fluka Capabilities And Cern Applications For The Study Of Radiation Damage To Electronics At High-Energy Hadron Accelerators", Progress In Nuclear Science And Technology, Vol. 2, p.948-954 (2011)
59. A. Mairani,S. Brons, F. Cerutti, A. Fassò, A. Ferrari, M. Krämer, K. Parodi, M.Scholz, F. Sommerer,"The FLUKA Monte Carlo code coupled with the local effect model for biological calculations in carbon ion therapy.", Physics in Medicine and Biology 55, 4273 2010

60. P.Schoofs, F.Cerutti, A.Ferrari, G.Smirnov,"Benchmark of the FLUKA model of crystal channeling against the UA9-H8 experiment"Nucl.Instrum.Meth. volume 355, (2015), Pages 374-377
61. M.N.Mazziotta, F.Cerutti, A.Ferrari, D.Gaggero, F.Loparco,P.R.Sala,"Production of secondary particles and nuclei in cosmic rays collisions with the interstellar gas using the FLUKA code" volume 81, (2016), p. 21-38
62. E. V. Bellinzona, M. Ciocca, A. Embriaco, A. Ferrari, A. Fontana, A. Mairani, K. Parodi, A. Rotondi, P. Sala and T. Tessonnier," A model for the accurate computation of the lateral scattering of protons in water" Physics in Medicine and Biology volume 61, 183 (2016)
63. C. Robert, G. Dedes, G. Battistoni, T. T. Böhlen, I. Buvat, F. Cerutti, M. P. W. Chin, A. Ferrari, P. Gueth, C. Kurz, L. Lestand, A. Mairani, G. Montarou, R. Nicolini, P. G. Ortega, K. Parodi, Y. Prezado, P. R. Sala, D. Sarrut and E. Testa "Distributions of secondary particles in proton and carbon-ion therapy: a comparison between GATE/Geant4 and FLUKA Monte Carlo codes",Physics in Medicine and Biology volume 58, 2879 (2013)
64. C. Theis, K. H. Buchegger, E. Feldbaumer, D. Forkel-Wirth, L. Jaegerhofer, S. Roesler And H. Vincke, "SimpleGeo – New Developments in the Interactive Creation and Debugging of Geometries for Monte Carlo Simulations",Nuclear Science and Technology, Vol. 2, pp.587-590 (2011)
65. Committee on a Scientific Assessment of Free-Electron Laser Technology for Naval Applications, National Research Council, Scientific Assessment of HighPower Electron Laser Technology. The National Academies Press, 2009, p. 30.
66. W.B. Colson, “Free Electron Laser Physics,” class notes for PH4055, Department of Physics, Naval Postgraduate School, summer 201.
67. A. Tsakanian, M. Dohlus, I. Zagorodnov,"Short range wake potentials of FLASH resistive tapered collimator and European XFEL undulator intersection", Nuclear Instruments and Methods in Physics Research A 659 (2011) 9–13.
68. W. Ackermann et al., Nature Photonics 1 (2007) 336.

69. P. Emma et al., First lasing and operation of an ångstrom-wavelength free-electron laser, Nat. Photonics 4, 641 (2010).
70. A. Bohnet, et al.,"Conditioning of the RF gun at the photo injector test facility at DESY Zeuthen", EPAC2002, La Villette-Paris, France, June 2002.
71. B. A. Grigoryan et al., Status of Areal RF Photogun Test Facility, Proc. of 5th International Particle Accel. Conf, Dresden, Germany, 2014, pp. 620-623.
72. H. N. Yeritsyan et al., The Interaction of Impurity Oxygen with Radiation Defects in Silicon Crystal, Journal of Modern Physics, 2015, 6, 2050-2057.
73. Vaclav Vylet and James C. Liu "Radiation protection at high-energy electron accelerators", SLAC Report SLAC-PUB- 9557, October 2002
74. Heinz Vincke, Stan Mao and Sayed Rokni, "FLUKA Calculations for the Shielding Design of the SPPS Project at SLAC", SLAC–PUB–10010 December 2003.
75. R.Rata, S.C.Lee, R.J.Barlow, "FLUKA simulations for radiation protection at 3 different Facilities", Proceedings of IPAC2016, Busan, Korea.
76. United Nations, Report of the United Nations Scientific Committee on the Effect of Atomic Radiation, General Assembly, Official Records A/63/46 (2008).
77. ICRP Publication 103, The 2007 Recommendations of the International Commission on Radiological Protection, Annals of the ICRP, Elsevier (2007).
78. ICRP, 2010. Conversion Coefficients for Radiological Protection Quantities for External Radiation Exposures, ICRP Publication 116, Annals of the ICRP 40(2-5).
79. G.F. Knoll, Radiation detection and measurements, Wiley (2010).
80. A. Wattenberg, "Nuclear Reactions at High-Energies" in Encyclopedia of Physics, Vol. XL (Springer, Berlin, 1957).
81. H. DeStaebler, T. M. Jenkins and W. R. Nelson, "Shielding and Radiation", Chapter 26 in The Stanford Two-Mile Accelerator, R. B. Neal, Editor (Benjamin, 1968).
82. A. Fasso, A. Ferrari and P. R. Sala, "Electron-photon Transport in FLUKA: Status" and A. Fasso, A. Ferrari, J. Ranft and P. R. Sala, "FLUKA: Status and Prospective for Hadronic Applications", in the Proceedings of the MonteCarlo 2000 Conference, Lisbon (October 23-26 2000).

83. M. E. Toms, “Bibliography of Photo- and Electronuclear Disintegrations”, U.S. Naval Research Laboratory Report Number NRL-BIB-24 (July 1965).
84. V. I. Antonesoc, “Photonuclear Reactions”, Bibliographical Series No. 10, International Atomic Energy Agency (1964).
85. H. W. Patterson and R. H. Thomas, Accelerator Health Physics (Academic Press, New York, 1973).
86. A hereto unpublished experiment, performed at SLAC in 1968 using a 10 GeV beam of positrons, currently provides us with our best knowledge of the ionizing radiation component (GamD) in the very-forward direction from a standard target. In this experiment, a fine-mesh matrix of tiny TLD rods (0.5 mm dia.), covering an angular interval of $0^0 – 5^0$, was centered 10-ft downstream of the target.
87. T. M. Jenkins, “Neutron and photon measurements through concrete for a 15 GeV electron beam on a target—comparison with models and calculations”, Nucl. Instr. Meth. 159 (1979) 265.
88. S. Roesler, et al., “Simulation of Remanent Dose Rates and Benchmark Measure- ments at the CERN-EU High Energy Reference Field Facility,” in Proceedings of the Sixth International Meeting on Nuclear Applications of Accelerator Technology, San Diego, CA, 1-5 June 2003, 655–662 (2003).
89. M. Caresana, et al., A new version of the LUPIN detector: Improvements and latest experimental verification, Review of Scientific Instruments 85, 065102 (2014).
90. F.A. Berends, R. Kleiss & S. Jadach, Radiative Corrections to Muon Pair and Quark Pair Production in Electron-Positron Collisions in the Z0 Region, Nucl. Phys. B202 (1982) 63–88
91. International Commission on Radiation Units and Measurements, Fundamental Quantities and Units for Ionizing Radiation, ICRU Report 60 (1998).
92. W. R. Nelson and T. M. Jenkins, "The SHIELD11 Computer Code", T.M.Jenkins, SLAC-R-737, UC-414
93. SwissFEL Radiation Protection Report for SwissFELCDR, FEL-FU96-008-0.

94. Theis C., Buchegger K.H., Brugger M., Forkel-Wirth D., Roesler S., Vincke H., " Interactive three dimensional visualization and creation of geometries for Monte Carlo calculations", Nuclear Instruments and Methods in Physics Research A 562, pp. 827-829 (2006)
95. A. Ioachim, M.I. Toacsan, M.G. Banciu, L. Nedelcu, F. Vasiliu, H.V. Alexandru, C. Berbecaru, G. Stoica, Prog. Solid State Chem. 35 (2007) 513–520.
96. Y. Ota, K.I. Kakimoto, H. Ohsato, T. Okawa, J. Eur. Ceram. Soc. 24 (2004) 1755–1760.
97. Y.C. Chen, P.S. Cheng, C.F. Yang,W.C. Tzou, Ceram. Int. 27 (2001) 809–813.
98. H. Zhou, H.Wang, Y. Chen, K. Li, X. Yao, Mat. Chem. Phys. 113 (2009) 1.
99. E.P. Gorzkowski, M.J. Pan, B. Bender, C.C.M. Wu, J. Electroceram. 18 (2007) 269–276.
100. H. Nikjoo, P.O'Neill, W.E.Wilson, D.T.Goodhead,Radiation Research 156(5 (Part 2))(2001)577.
101. D.T.Goodhead, International Journal of Radiation Biology 65(1)(1994)7.
102. J.F.Ward, Progressin Nucleic Acid Research Molecular Biology 35 (1988)95.
103. M. Kramer, W.K.Weyrather, M.Scholz, Technology in Cancer Research and Treatment 2(5) (2003) 427.
104. M.B. Vrouenraets, G.W.Visser, G.B.Snow, G.A.van Dongen, Anticancer Research 23(1B) (2003) 505.